Modelling weathering processes at the catchment scale: The WITCH numerical model

Yves Godderis, Louis François, Anne Probst, Jacques Schott, David Moncoulon, David Labat, Daniel Viville

▶ **To cite this version:**

Yves Godderis, Louis François, Anne Probst, Jacques Schott, David Moncoulon, et al.. Modelling weathering processes at the catchment scale: The WITCH numerical model. Geochimica et Cosmochimica Acta, 2006, 70, pp.1128-1147. ⟨10.1016/j.gca.2005.11.018⟩. ⟨hal-00665423⟩

HAL Id: hal-00665423

https://hal.science/hal-00665423v1

Submitted on 20 Feb 2013

HAL is a multi-disciplinary open access archive for the deposit and dissemination of scientific research documents, whether they are published or not. The documents may come from teaching and research institutions in France or abroad, or from public or private research centers.

L'archive ouverte pluridisciplinaire **HAL**, est destinée au dépôt et à la diffusion de documents scientifiques de niveau recherche, publiés ou non, émanant des établissements d'enseignement et de recherche français ou étrangers, des laboratoires publics ou privés.

HAL Authorization

Available online at www.sciencedirect.com
SCIENCE DIRECT
Geochimica et Cosmochimica Acta 70 (2006) 1128–1147
Geochimica
www.elsevier.com/locate/gca

Modelling weathering processes at the catchment scale: The WITCH numerical model

Yves Goddéris [a,*], Louis M. François [b], Anne Probst [a], Jacques Schott [a], David Moncoulon [a], David Labat [a], Daniel Viville [c]

[a] Laboratoire des Mécanismes et Transferts en Géologie, Observatoire Midi-Pyrénées, CNRS, Toulouse, France
[b] Laboratoire de Physique Atmosphérique et Planétaire, Université de Liège, Belgium
[c] Centre de Géochimie de la Surface, Strasbourg, France

Received 8 April 2005; accepted in revised form 4 November 2005

Abstract

A numerical model of chemical weathering in soil horizons and underlying bedrock (WITCH) has been coupled to a numerical model of water and carbon cycles in forest ecosystems (ASPECTS) to simulate the concentration of major species within the soil horizons and the stream of the Strengbach granitic watershed, located in the Vosges Mountains (France). For the first time, simulations of solute concentrations in soil layers and in the catchment river have been performed on a seasonal basis. The model is able to reproduce the concentrations of most major species within the soil horizons, as well as catching the first-order seasonal fluctuations of aqueous calcium, magnesium and silica concentrations. However, the WITCH model underestimates concentrations of Mg^{2+} and silica at the spring of the catchment stream, and significantly underestimates Ca^{2+} concentration. The deficit in calculated calcium can be compensated for by dissolution of trace apatite disseminated in the bedrock. However, the resulting increased Ca^{2+} release yields important smectite precipitation in the deepest model layer (in contact with the bedrock) and subsequent removal of large amount of silica and magnesium from solution. In contrast, the model accurately accounts for the concentrations of major species (Ca, Mg and silica) measured in the catchment stream when precipitation of clay minerals is not allowed. The model underestimation of Mg^{2+} and H_4SiO_4 concentrations when precipitation of well crystallized smectites is allowed strongly suggests that precipitation of well crystallized clay minerals is overestimated and that more soluble poorly crystallized and amorphous materials may be forming. In agreement with observations on other watersheds draining granitic rocks, this study indicates that highly soluble trace calcic phases control the aqueous calcium budget in the Strengbach watershed.
© 2005 Elsevier Inc. All rights reserved.

1. Introduction

Since the early work by Walker et al. (1981), continental silicate weathering has been recognized as a major controlling factor of the geological carbon cycle, and hence of climate (Goddéris and François, 1995; Kump and Arthur, 1997; Kump et al., 2000; Berner and Kothavala, 2001; Donnadieu et al., 2004; Goddéris and Joachimski, 2004). Even at shorter timescales, there is a growing interest in fluctuations of large scale consumption of atmospheric CO_2 during the recent glacial–interglacial cycles (Munhoven, 2002), as well as in the present-day global warming induced by human activities. For instance, the GEM-CO_2 model, which calculates the weathering rates with a 1° latitude × 1° longitude on the basis of simple parametric laws linking large scale runoff to rock weathering (Amiotte-Suchet et al., 2003), has been coupled to a 3D model of carbon transport within the ocean to evaluate the impact of the continental alkalinity input on the present-day inter-hemispheric CO_2 signal (Aumont et al., 2001).

Nevertheless, recent extensive field studies performed on small and large scale watersheds have shown that the behaviour of large scale (large scale in the sense of

* Corresponding author.
E-mail address: godderis@lmtg.obs-mip.fr (Y. Goddéris).

0016-7037/$ - see front matter © 2005 Elsevier Inc. All rights reserved.
doi:10.1016/j.gca.2005.11.018

watershed scale) silicate weathering is more complex than the rather simple runoff (and possibly temperature) dependence used until now (most of them rely on the Brady and Carroll (1994) and White and Blum (1995) studies). Although standard temperature-runoff parametric laws generally apply to basaltic lithologies (Dessert et al., 2001, 2003), the relationship between temperature, runoff and CO_2 consumption for granitic lithologies is much more variable and complex (Oliva et al., 2003). Moreover, it has been shown that trace minerals may play a fundamental role in base cations release and atmospheric CO_2 consumption by granitic lithologies. For instance, Oliva et al. (2004) have shown that trace minerals (mainly trace calcic phases) account for 80–90% of the calcium flux exported from a high mountain watershed. Blum et al. (2002) reported that about 35% of the Ca exported from the Hubbard Brook catchment likely came from trace apatite dissolution.

A main challenge for the accurate description of continental weathering is to identify the main factors controlling chemical weathering and to quantify their effect in given environments and at various geometric and time scales. A critical step to rise to this challenge is the building of a numerical model describing the large-scale (watershed-scale) weathering of silicate rocks, based on a description of the weathering processes as mechanistic as possible (including dissolution of primary and secondary minerals and precipitation of secondary minerals, in interaction with continental vegetation and coupled to hydrological processes). Mechanistic models already exist that work at the square-meter-scale in natural environments and are capable of describing weathering processes down to approximately the root depth. For instance, kinetic models such as the KINDIS code (Madé et al., 1994) have been used in an attempt at describing mineral dissolution in natural environment (Probst et al., 2000). Among those models, the pioneering and most complete one is surely the SAFE model developed by Sverdrup and Warfinge (1995) that has been tested and validated for many locations and has been upscaled in several countries to create regional weathering maps. This model, however, has been essentially used to describe critical loads and soil acidification in natural ecosystems and not within the scope of predicting the geochemical cycling of elements, including carbon, during weathering. Furthermore, it may be not appropriate to estimate weathering in deep soil profiles since it does not explicitly incorporate the calculation of chemical affinities and secondary mineral precipitation which may be critical, particularly below the root zone where solutions become supersaturated with respect to both primary and secondary minerals. It should be noted that recent developments of the SAFE model lead to the building up of an integrated model of soil and vegetation processes in forest ecosystems (ForSAFE) working at the centennial timescale (Wallman et al., 2005, 2002), designed for sustainability assessments.

We propose here a first step towards the establishment of a mechanistic numerical model of silicate weathering operating at the catchment scale, through the numerical coupling of a new weathering model (WITCH) and a model of water and carbon cycles in forest ecosystems (ASPECTS, Rasse et al. (2001)). It must be kept in mind that given the variety of processes that must be accounted for, this study presents only a first effort towards this goal. The originality of our approach lies in the direct comparison of the results of this model on a seasonal timescale with the data acquired on a monolithological granitic catchment located in the Vosges Mountains in France (the Strengbach watershed). This watershed represents an ideal site for an upscaling study since hydrological and geochemical data are available for several soil profiles (from October 1994 to October 1995 with a 15 day timestep), for a spring collector (catching the four main springs of the main stream) and for the main stream itself (from 1985 to 1998 with a weekly timestep). Furthermore, the 1994–1995 year can be considered as a typical period on an hydrological point of view, since the total rainfall (1397 mm) is very close to the mean rainfall calculated over 13 years of data acquisition (1320 mm). Soil solutions sampled at different depths will be used to validate the geochemical sub-model (including kinetic mineral dissolution and precipitation), while data from spring collectors can be used as a validation of the upscaling procedure. Finally, it should be kept in mind that this catchment was also intensively studied because of large pollutant input through atmospheric deposition. Such input strongly perturbates the natural system and should thus be incorporated in the model. Modelling this perturbation is probably a challenge for the future, but it is already partly considered within this preliminary work since seasonal fluctuations in atmospheric acidic deposition are accounted for.

2. Model description

2.1. The WITCH model

The WITCH geochemical model is a box model that integrates the chemical composition of n boxes representing the soil solution as a function of time (n can be defined depending on the field configuration). The mass balance is calculated for each box at each timestep:

$$\frac{dC}{dt} = F_{top} - F_{bottom} + F_{weath} + F_{exchange} - F_{prec}, \quad (1)$$

where C is the box content for a given species (Ca^{2+}, Mg^{2+}, K^+, Na^+, $\Sigma SiO_2(aq)$, ΣAl, SO_4^{2-}, ΣPO_4 and acid neutralizing capacity). NH_4^+ and NO_3^- are not explicitly modelled, and are simply accounted as proton suppliers. F_{top} represents the input flux at the top of the considered box through drainage while F_{bottom} is the output flow at the base of the box. F_{weath} represents the input of elements from dissolution of primary and secondary minerals. $F_{exchange}$ could be either positive or negative, and accounts for cation exchange between the soil solution and the clay-humic exchange complex, and F_{prec} represents the removal of elements through the precipitation of secondary

minerals. Three additional differential equations are written to calculate the fraction of sites on the exchange complex occupied by, respectively, Ca^{2+}, Mg^{2+} and K^{+}. We did not include any exchange of Na^{+}. The exchange processes are described assuming a Fick diffusion law (Sverdrup and Warfinge, 1995), and are thus described in a fully dynamic way:

$$\frac{dE_{BC}}{dt} = -k_x \cdot (BC_{surf} - BC_{sol}), \quad (2)$$

where E_{BC} is the fraction of sites occupied by a given base cation BC (Ca^{2+}, Mg^{2+} or K^{+}), BC_{sol} is the concentration of the base cation in the soil solution calculated at time t, and BC_{surf} is the concentration of BC at the exchange surface. BC_{surf} are calculated as a function of the H^{+} concentration at the surface, itself estimated from the acid neutralizing capacity (ANC) change between the solution and the exchange complex during the exchange process (Alveteg, 1998). The cation exchange capacity (CEC) is held constant within each soil layer. Finally, k_x is a mass transfer coefficient (Warfinge and Sverdrup, 1998).

Dissolution of primary and secondary minerals is described through kinetic laws derived from transition theory concept (Eyring, 1935). Overall dissolution rates R_S are assumed to be the sum of H^{+}, OH^{-}, H_2O and organic ligands promoted dissolution:

$$R_S = A \cdot \left[\sum_i k_i \exp\left(\frac{-E_a^i}{RT}\right) \cdot a_i^{n_i} \cdot f_{inh} \right] (1 - \Omega^s), \quad (3)$$

where A stands for the mineral reactive surface (m^2/m^3 of soil), k_i and E_a^i are the dissolution rate constant and the activation energy for the i species promoted dissolution, and a_i and n_i stand for the activity of species i and the order of reaction with respect to i, respectively, and f_{inh} describes the inhibiting effect of aqueous species on mineral dissolution. In this study Al^{3+} is considered as the main inhibiting species and the expression of f_{inh} has been derived from Oelkers et al. (1994), Schott and Oelkers (1995) and Devidal et al. (1997). No provision has been made for a possible catalysis of dissolution rates by CO_2 aqueous species since Golubev et al. (2005) have recently shown that these species have no direct effect on silicate dissolution rates. The consequence of departure from equilibrium on mineral dissolution/precipitation rate is accounted by the $(1 - \Omega^s)$ term, where Ω stands for the solution saturation index with respect to the particular solid and s is a stoichiometric number. Dissolution or precipitation occur depending if this function is positive or negative. WITCH does not include a nucleation model, and precipitation rate is assumed to be proportional to the reactive surface area of the mineral, an input parameter calculated from the observed relative abundance of minerals in each soil layer, and from the soil texture. As a consequence, only already present secondary minerals are able to precipitate, a reasonable assumption for a study that assumes the catchment is close to steady-state. The WITCH model includes kinetic laws for 31 minerals. Kinetic data for the minerals included in the present study are listed in Table 1. Solubility products of primary and secondary minerals along with the enthalpy of their dissolution reactions are listed in Table 2.

The differential system is solved using a method adapted from the fully implicit Runge-Kutta 6th order method, with adaptative time step. The output are then injected at each time step into the speciation module that calculates the complete speciation of the solution for 17 chemical species (H^{+}, OH^{-}, HCO_3^{-}, CO_3^{2-}, H_2CO_3, Al^{3+}, $AlOH^{2+}$, $Al(OH)_2^{+}$, $Al(OH)_4^{-}$, H_4SiO_4, $H_3SiO_4^{-}$, $H_2SiO_4^{2-}$, R^{-} standing for organic acid functional group, PO_4^{3-}, HPO_4^{2-}, $H_2PO_4^{-}$, H_3PO_4). Reactions among aqueous species are assumed to occur instantaneously. Values of their equilibrium constants and enthalpies of reaction are taken from the SUPCRT database, except for Al aqueous species taken from (Castet et al., 1993; Wesolowski and Palmer, 1994).

2.2. Coupling with a model of water and carbon cycles in forest ecosystems

Several inputs of the WITCH model are unmeasurable. This is particularly the case for the vertical water fluxes and volumetric water contents at seasonal scale. Also element exchanges between soil solution and biological reservoirs throughout the soil horizons are required from day-to-day in order to perform seasonal runs. Finally, soil and below soil CO_2 partial pressure were never measured on site. All these forcing functions (with an hourly time resolution) are calculated offline using the ASPECTS model (Rasse et al., 2001) (Fig. 1). Atmosphere-soil-plant exchanges of carbon in temperate Sylvae (ASPECTS) is a fully coupled scheme of the water and carbon cycles in the vegetation and soils of temperate forest ecosystems. The version used here does not contain nitrogen or other nutrient cycles. All fluxes and pools are calculated with a time step of 2 min. This very short time step was necessary for the calculation of CO_2 diffusion within the soil to be stable. Hourly meteorological data (air temperature, precipitation, global radiation, air relative humidity and wind speed) measured at the site were linearly interpolated at the model time step. Photosynthesis and transpiration are calculated separately for shaded and sunlit leaves (De Pury and Farquhar, 1997). The stomatal conductances of CO_2 and H_2O are related to the net assimilation of the leaves (Leuning, 1995). Photosynthetic assimilates transit through a carbohydrate pool before being allocated to other plant reservoirs (leaf, starch, branches, stem, coarse roots and fine roots). This allocation varies with stress factors (water, temperature, soil strength and soil aeration) influencing the development of forest vegetation. Growth rate of each plant carbon reservoir is given as the difference between carbon allocation and the carbon lost in respiration and litter production. The model can be integrated over several decades to simulate the growth of the trees. No heat budget is calculated at the surface, so that soil surface and leaf temperatures are assumed to be equal to the measured air temperature. All

Table 1
Kinetic dissolution constants at 25 °C (mol/m^2/s) and activation energy (kJ/mol) of the dissolution reactions promoted by H^+, OH^-, water (w) and organic ligands (L), as used in the WITCH model. Also shown is the reaction order with respect to H^+ and OH^- promoted dissolution (n_H, n_{OH}). Symbol ~ stands for "no effect".

	pk_H E_aH n_H	pk_{OH} E_aOH n_{OH}	pk_W E_aw	pk_L E_aL
Albite (An_6)[a]	9.50 60 0.5	9.95 50 0.3	12.60 67	12.96 59
Orthoclase[b]	9.65 60 0.5	10.70 50 0.3	12.85 67	~ ~
Quartz[c]	~ ~ ~	11.00 85 0.25	13.40 85	~ ~
Muscovite[d]	12.20 22 0.17	11.71 22 0.16	~ ~	~ ~
Biotite[e]	10.88 35 0.32	~ ~ ~	14.20 35	~ ~
Kaolinite[f]	12.45 50 0.38	10.74 40 0.73	14.43 55	~ ~
Apatite[g]	5.08 34.7 0.87	~ ~ ~	~ ~	~ ~
All montmorillonites[h]	9.8 48 0.38	~ ~ ~	13.9 55	12.1 48.3
Illite[i]	11.7 46 0.6	12.3 67 0.6	15 14	12.3 48.3

[a] Fitting within the framework of Eq. (3) of data reported by Blum and Stillings (1995) for albite. In agreement with these authors, it was assumed that the anorthite content (An_6) did not modify albite dissolution rate.
[b] Fitting of data reported by Blum and Stillings (1995) for orthoclase.
[c] Dove (1994).
[d] Fitting of data reported by Nagy (1995) for muscovite (pH $\leqslant$ 8).
[e] Fitting of data reported by Nagy (1995) for biotite.
[f] Fitting of data reported by Nagy (1995) for kaolinite.
[g] Fitting of data for fluoroapatite (pH $\leqslant$ 7.5) from Guidry and Mackenzie (2003) and Chaïrat (2005).
[h] Holmqvist (2001).
[i] Köhler et al. (2003).

evaporative fluxes involved in the surface water budget are calculated from the saturation deficit using a resistance formalism. Precipitation interception by the foliage is represented by a reservoir which can be filled up to a maximum level. The proportion of wet foliage (φ_{wet}), i.e., which contributes to the evaporation of intercepted water, is proportional to the size of this interception reservoir. When the maximum level is reached ($\varphi_{wet} = 1$), any excess water is evacuated as throughfall. Snow can accumulate in a surface reservoir. Precipitation is assumed to be snowfall when air temperature is below 0 °C. Outputs from the snow reservoir are represented by snow melt, which is a linear function of air temperature and snow evaporation. Potential infiltration of water into the soil is the sum of direct precipitation (i.e., precipitation which reaches the ground without being intercepted by the foliage), throughfall (i.e., any excess water from the interception reservoir) and snow melt. Surface runoff occurs when potential infiltration exceeds the maximum amount of water that can be evacuated by vertical drainage from a small surface water reservoir (5 mm layer with textural characteristics of the first soil layer). Soil evaporation is assumed to occur within this surface layer and is calculated using a resistance at the soil surface based on the work of Mahfouf and Noilhan (1991). Actual infiltration of water into the soil is then obtained as the difference between potential infiltration and the sum of surface runoff and soil evaporation.

The soil is divided into 6 layers along the vertical dimension consistently with the WITCH run design (see next section). Temperature, water content and PCO_2 are calculated in each soil layer, as well as coarse and fine root biomass, litter and soil carbon amounts. Temperature is calculated by solving the heat diffusion equation assuming, as boundary conditions, that temperature is equal to the measured surface air temperature at the soil surface and to its measured annual mean surface temperature at the bottom of the lowest soil layer. Soil water content is computed by solving Richards' equation (Viterbo and Beljaars, 1995), setting the vertical water flux to the infiltration rate at the soil surface and imposing free drainage at the bottom. Soil textural data (% sand, % silt, % clay) must be provided by the user for each soil layer. Soil PCO_2 is calculated from the CO_2 production rate (soil microbial respiration + root respiration) in each layer and by solving the diffusion equation (Fang and Moncrieff, 1999) with PCO_2 set to the atmospheric value at the soil surface and a zero flux boundary condition at the bottom of the model soil.

The ASPECTS model has been successfully tested on two Belgian forested sites (Vielsalm and Braschaat), where it was shown to be able to simulate the net ecosystem exchange for several years of data (Rasse et al., 2001). Importantly, one of these sites (Vielsalm) has a similar forest cover (beech trees and Douglas firs) to the Strengbach (beech and Norway spruce trees) and exhibits similar temperatures and precipitation conditions.

2.3. Sites, run design, forcing functions and parameters

The Strengbach forested catchment (80 ha area) is located on the eastern part of the Vosges Mountains (North East of France), 58 km SW from Strasbourg. The elevation ranges from 883 m at the outlet to 1146 m at the catchment divide. The slopes are rather steep. The climate is temperate oceanic mountainous and westerly winds dominate. The monthly average of daily mean temperature ranges from −2 to 14 °C (Probst et al., 1990). The mean annual rainfall is about 1400 mm (Probst and Viville, 1997). Most of the rainfall occurs in

Table 2
Equilibrium constants at 25 °C and enthalpies of reaction for dissolution of minerals involved in the present study

	Dissolution reaction	pK_{eq}	ΔH^0_R (kJ/mol)
Albite An 6%	Assimilated to albite: $NaAlSi_3O_8 + 4H_2O + H^+ \rightarrow Na^+ + Al^{3+} + 3H_4SiO_4$ + calcium release	−2.29	−73.82
Orthoclase	$KAlSi_3O_8 + 4H_2O + 4H^+ \rightarrow K^+ + Al^{3+} + 3H_4SiO_4$	0.022	−49.93
Quartz	$SiO_2 + 2H_2O \rightarrow H_4SiO_4$	3.98	25.06
Muscovite[a]	$KAl_3Si_3O_{10}(OH)_2 + 10H^+ \rightarrow K^+ + 3Al^{3+} + 3H_4SiO_4$	−12.70	−248.4
Biotite[b]	$KMg_{1.5}Fe_{1.5}AlSi_3O_{10}(OH)_2 + 10H^+ \rightarrow K^+ + 1.5Mg^{2+} + 1.5Fe^{2+} + Al^{3+} + 3H_4SiO_4$	−32.87	−55.6
Kaolinite[a]	$Al_2Si_2O_5(OH)_4 + 6H^+ \rightarrow 2Al^{3+} + 2H_4SiO_4 + 2H_2O$	−7.43	−147.7
Halloysite[a]	$Al_2Si_2O_5(OH)_4 + 6H^+ \rightarrow 2Al^{3+} + 2H_4SiO_4 + 2H_2O$	−12.5	−166.6
Gibbsite[a]	$Al(OH)_3 + 3H^+ \rightarrow Al^{3+} + 3H_2O$	−7.74	−105.3
$Gibbsite_{(amorphous)}$[a]	$Al(OH)_3 + 3H^+ \rightarrow Al^{3+} + 3H_2O$	−10.8	−110.9
Apatite[c]	$Ca_{10}(PO_4)_6F_2 + 12H^+ \rightarrow 10Ca^{2+} + 6H_2PO_4^- + 2F^-$	−49.99	−110.0
Ca-montmoril	$Si_4O_{10}(OH)_2Mg_{0.33}Al_{1.67}Ca_{0.165} + 6H^+ + 4H_2O \rightarrow 4H_4SiO_4 + 1.67Al^{3+} + 0.33Mg^{2+} + 0.165Ca^{2+}$	−2.53	−81.65
Na-montmoril	$Si_4O_{10}(OH)_2Mg_{0.33}Al_{1.67}Na_{0.33} + 6H^+ + 4H_2O \rightarrow 4H_4SiO_4 + 1.67Al^{3+} + 0.33Mg^{2+} + 0.33Na^+$	−2.58	−74.70
Mg-montmoril	$Si_4O_{10}(OH)_2Mg_{0.33}Al_{1.67}Mg_{0.165} + 6H^+ + 4H_2O \rightarrow 4H_4SiO_4 + 1.67Al^{3+} + 0.50Mg^{2+}$	−2.49	−86.44
K-montmoril	$Si_4O_{10}(OH)_2Mg_{0.33}Al_{1.67}Na_{0.33} + 6H^+ + 4H_2O \rightarrow 4H_4SiO_4 + 1.67Al^{3+} + 0.33Mg^{2+} + 0.33K^+$	−2.24	−69.66
Illite[d]	$Si_{3.4}O_{10}(OH)_2Mg_{0.02}Al_{2.38}Ca_{0.01}K_{0.44} + 7.64H^+ + 2H_2O \rightarrow 3.4H_4SiO_4 + 2.38Al^{3+} + 0.02Mg^{2+} + 0.01Ca^{2+} + 0.44K^+$	−6.82	−146.31

Unless otherwise specified, data for minerals and aqueous species are from SUPCRT (SPEQ03.DAT) except for Al^{3+} (Castet et al., 1993; Wesolowski and Palmer, 1994) and H_4SiO_4 (Walther and Hegelson, 1977).

[a] Drever (1997).

[b] Biotite Gibbs free energy calculated in this study assuming a regular solid solution between annite and phlogopite (Fe atomic fraction in M1 sites of 0.9 and W = 9 kJ, THERMOCALC) and end-members thermodynamic data from SUPCRT.

[c] Guidry and Mackenzie (2003).

[d] Illite Gibbs free energy calculated in this study based on the electronegativity scale method (Vieillard, 2000).

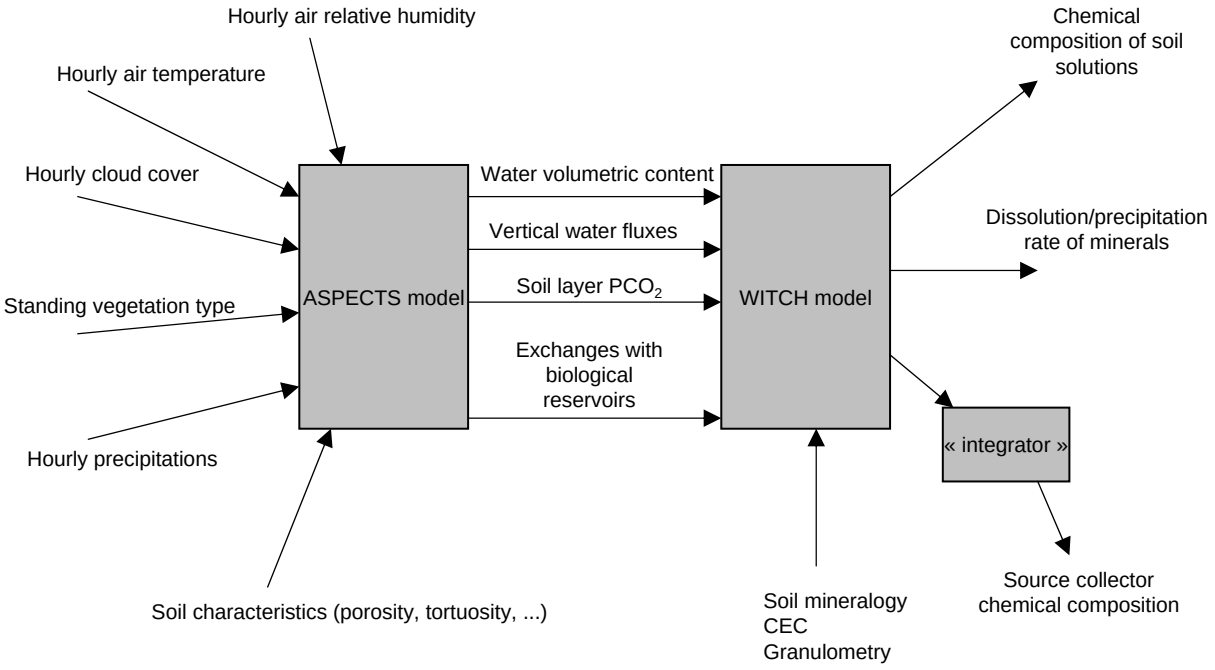

Fig. 1. Schematic view of the coupling between the ASPECTS biospheric model and the WITCH geochemical model, including the main forcing functions of ASPECTS, and the output of WITCH. The coupling is based on an hourly timescale.

spring whereas the driest season is in autumn. The total runoff averages 853 mm for the 1986–1995 period (Probst et al., 1995), which corresponds to a mean annual discharge of 21.7 L/s. The bedrock is a base poor leucogranite (the Brézouard granite) aged of 315 ± 7 Ma (Bonhomme, 1967). This granite is coarse grained and has undergone hydrothermal alteration 183.9 My ago, which is particularly obvious on the south-facing slope of the catchment (El Gh'Mari, 1995). Hydrothermal alteration has caused depletion of plagioclase, and precipitation of illite and hematite in the fractured granite. At the upper margin of the catchment, a banded gneiss lies in contact with the granite. The soils are rather deep (80 cm in average), sandy and stony and overlay a saprolite, which can reach 10 m depth in places. They belong to the brown acidic to ochreous podzolic soils series.

Both sides of the catchment have been equipped with an experimental site (respectively, PP on the south-facing slope, and HP on the north-facing slope of the catchment). Both sites are characterized by a granitic mineralogy (Brezouard granite). Mineral composition of the soil layers for both sites are shown in Fig. 2. The relative abundance of octahedral Ca-, Na-, Mg- and K-montmorillonites within the montmorillonite pole is not known, and we assume that all the four different montmorillonites are equally abundant (1/4 of the total smectite abundance). Note that apart from the mineralogical composition of montmorillonites, the exchangeable cation pool is dominated by the H^+ and Al^{3+} cations, particularly within the upper soil layers, due to the atmospheric acidic input. The vegetation consists in 130-year-old beech trees (HP), which cover about 20% of the catchment surface and are exclusively located on the northern flank, and in 80-year-old spruces (PP) covering the remaining 80% of the catchment. The PP site is located on the slightly hydrothermalized part of the catchment.

Separate model simulations have been performed on the HP and PP sites, assuming that they ideally represent the two mineralogical and ecological poles of the Strengbach (HP for the non hydrothermalized granite below beech trees and PP for the hydrothermalized granite below spruces). Indeed, even for a monolithological catchment, the mineralogy is a function of the geomorphology, the vegetation cover, the exposure and the hydrothermal

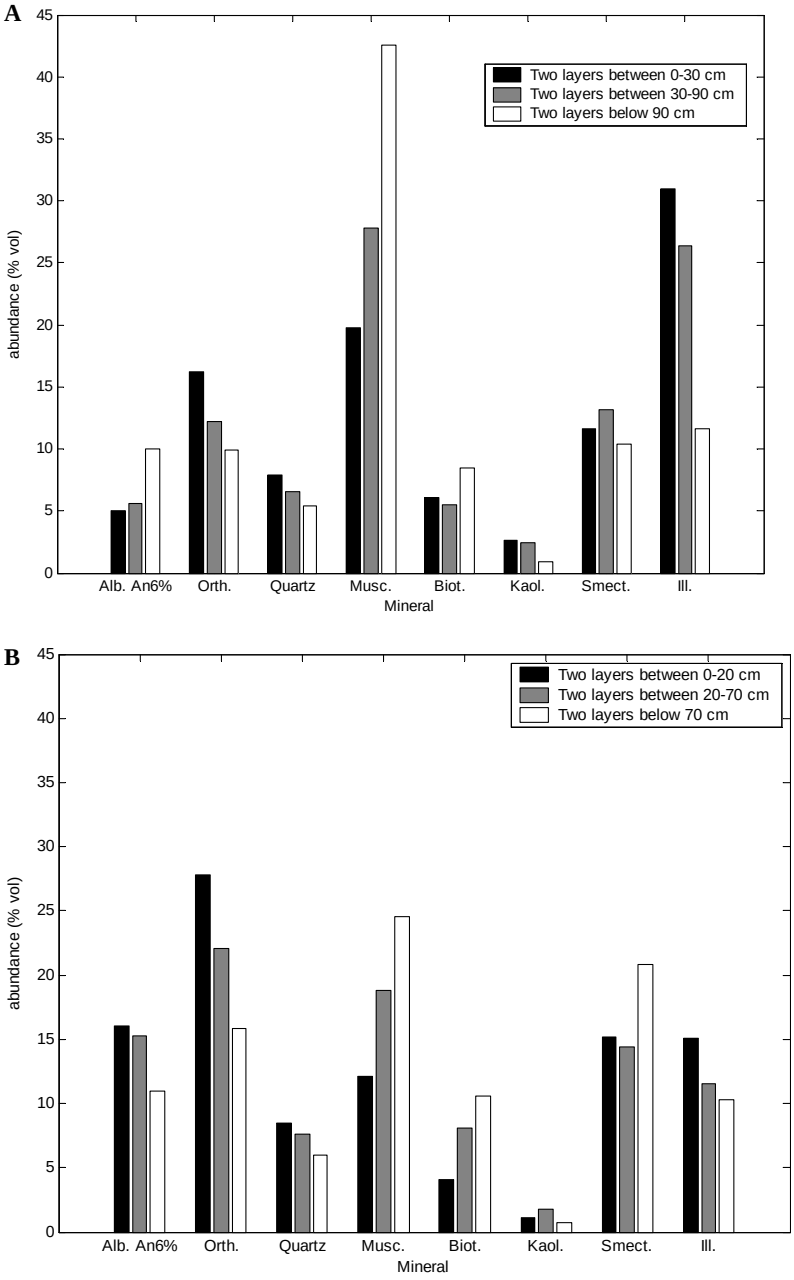

Fig. 2. Mineralogy for sites (A) PP and (B) HP used in the simulations. The reference run was performed without apatite.

history. This is why all simulations were doubled (HP and PP) to account for this variability, and to ensure that the upscaling procedure to the whole catchment based on the results obtained for the PP and HP sites is valid. The soil profile is represented by 6 layers in the ASPECTS and WITCH models, extending down, respectively, to 150 (HP) and 180 cm (PP). The layers have been defined following Fichter (1997). Soil characteristics, including texture and density, are summarized in Table 3. Soil solutions were sampled and analyzed from October 1994 to October 1995 at 10 and 60 (PP) or 70 (HP) cm depth, with a two week sampling interval (Probst et al., 2000). These measurements include major cations, aluminium, aqueous silica and SO_4^{2-} concentrations. Throughfall chemical compositions have been measured with a 15-day sampling interval for each site. DOC content is fixed within each layer (Table 3) in agreement with the estimations from Dambrine et al. (1995). Mineral reactive surface area A (m^2/m^3) has been calculated from soil texture (Table 3), according to a parametric law (Sverdrup and Warfinge, 1995) as an approach of the BET surface (Hodson et al., 1998):

$$A = (8.0x_{clay} + 2.2x_{silt} + 0.3x_{sand} + 0x_{coarse}) \cdot \rho, \quad (4)$$

where x_{clay}, x_{silt}, x_{sand} and x_{coarse} represent the textural fractions of the soils, respectively, clay, silt, sand and coarse materials so that $x_{clay} + x_{silt} + x_{sand} + x_{coarse} = 1$. ρ is the soil density in g/m^3 (Table 3). As noted by Gautier et al. (2001) and Sverdrup and Warfinge (1995), the actual reactive surface might be lower than this total surface, but there is no real standard method to fix the reactive surface of the minerals. So using the parametric law appears to be the only alternative. The relative ratio between the BET and the effective reactive surface is a specific property of the mineral investigated which is generally not known. Coherence of calculations performed in this study was ensured by normalizing all mineral dissolution rate constants to BET surface area.

Reactive surface area is distributed among the various minerals according to their volume abundance, itself calculated from the weight abundance measured within the 6 top layers (Fichter et al., 1998a). The texture as a function of depth is taken from Aubert (2001), and the relative proportions of clay, silt and sand materials used in the model are given in Table 3. CEC is fixed to the following values for the first four layers from top to bottom: 7.86×10^{-5}, 7.70×10^{-5}, 5.02×10^{-5} and 1.79×10^{-5} keq/kg (Fichter, 1997). Below layer 4, CEC is estimated through linear extrapolation. Finally, Gapon exchange constant are taken from Posch et al. (2003). The constants given for sandy, silt and clay soils are weighted by the measured texture for each layer.

Hourly meteorological data measured from October 1994 to September 1995 are used to force the models. ASPECTS is integrated over the lifetime of the trees from seedlings to the current adult forest by forcing each year of model-time with the 1994–1995 meteorological dataset. The daily runoff predicted by the hydrological sub-model of ASPECTS is compared in Fig. 3 to the runoff derived from the measured stream discharge. The overall shape and amplitude of the model runoff curve is relatively satisfactory compared to the data. However, it must be stressed that the model runoff corresponds to the vertical drainage at the bottom of the deepest model soil layer (at HP or PP sites), whereas the data represent daily stream discharge. The peaks of these two quantities may be significantly out of phase due to the existence of a saturated zone near the outlet of the Strengbach catchment (which reacts rapidly to rainfall), as well as to potential water storage in underground reservoirs. Fig. 4 shows the PCO_2 calculated by ASPECTS in the different soil layers of HP and PP sites. Soil PCO_2 was not measured on site, so that this critical parameter cannot be strictly validated. On a mean annual basis, calculated PCO_2 reaches, respectively, 3.35 and 7 times the atmospheric pressure of 320×10^{-6}

Table 3
Percentage of clay/silt/sand of the reactive minerals as a function of depth for HP and PP horizons

Layers (cm)	% Clay	% Silt	% Sand	Density (g/m^3)	Total mineral reactive surface (10^6 m^2/m^3)	DOC content (mg/L)
HP horizon						
0–10	20.3	18.6	7.6	1000×10^3	2.06	20
10–20	14.4	16.9	6.8	1700×10^3	2.62	15
20–45	11.0	16.9	5.1	1350×10^3	1.71	5
45–70	7.6	16.9	8.5	1500×10^3	1.50	1
70–100	8.5	25.4	10.2	1700×10^3	2.15	1
100–150	6.8	28.8	10.2	1700×10^3	2.05	0
PP horizon						
0–10	14.9	15.4	4.3	1300×10^3	1.54	20
10–30	17.1	13.7	6.8	1500×10^3	2.87	15
30–60	18.8	15.4	6.8	1700×10^3	2.51	5
60–90	17.9	16.2	7.7	1500×10^3	2.72	1
90–120	17.1	13.7	6.0	1800×10^3	2.88	1
120–180	11.1	9.4	6.0	2000×10^3	1.89	0

Also mentioned is the mineral reactive surface and the DOC content.

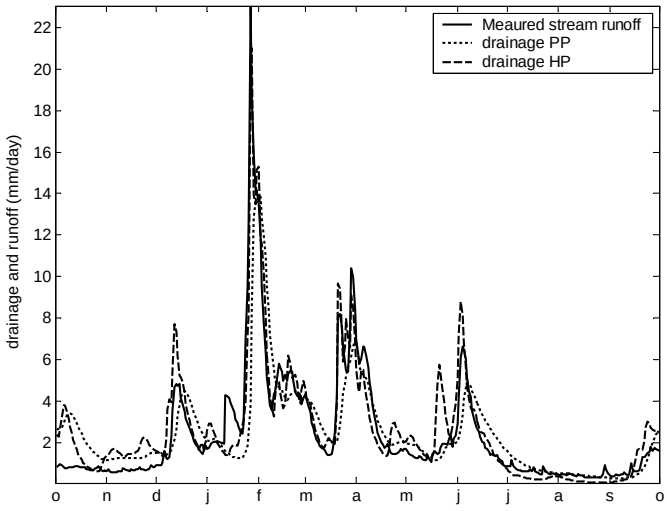

Fig. 3. The Strengbach runoff as measured at the site between October 1994 and September 1995 and compared to the drainage calculated by ASPECTS at the bottom of the deepest model soil layer for HP and PP sites.

atmosphere (this atmospheric value corresponds to the CO_2 pressure calculated at the average elevation of the site; it is assumed constant in time over the whole simulation) for the HP and PP lowest soil horizons, respectively (layer 6, 100–150 and 120–180 cm depth, respectively). Uptake of Ca^{2+}, Mg^{2+}, K^+, phosphorus and sulfur by vegetation is assumed proportional to the gross primary productivity calculated by ASPECTS and the measured mean Ca/C (1.12×10^{-3} mol/mol), Mg/C (2.54×10^{-4} mol/mol), K/C (6.11×10^{-4} mol/mol), P/C (1.41×10^{-4} mol/mol) and S/C (2.23×10^{-3} mol/mol) in the catchment living trees older than 80 years. Release of these elements is calculated proportionally to the release of carbon through oxidation of organic carbon, itself calculated by the ASPECTS model within each soil horizon. The net annual exchange of cations between vegetation and soil solutions is assumed to be equal to zero (steady-state ecosystem). Furthermore, this steady-state hypothesis also implies that the seasonal base saturation on the exchange complex fluctuates around a constant mean value, with no long term trend. The only impact of the exchange complex on the model results is a dampening of the calculated seasonal fluctuations of the base cation concentrations in soil solution (except for Na^+ that is not adsorbed on the exchange complex).

A deep layer box (layer 7, Fig. 5) has been added within the WITCH model on both HP and PP site, from, respectively, 1.5 to 10 m, and 1.8 to 10 m. This deep box accounts for deep weathering processes within the catchment, where the bedrock is in contact with percolating solutions. DOC within the deep box is fixed to 0 mg/L, and soil PCO_2 to a constant value equal to the mean annual value within the deepest soil horizon (layer 6). The value of layer 7 temperature is fixed to the catchment annual mean air temperature. Soil water content and vertical water fluxes are assumed to be the same as in layer 6 (the ASPECTS model runs do not extend so deep). As a result, the mean residence time of water within layer 7 is about 8 months. Similarly, mineralogy and grain size distribution within this deep box is assumed to be the same as in layer 6.

A first set of WITCH simulations have been performed on both HP and PP locations. The initial conditions for each run are calculated through a 20-year run with mean annual temperature, atmospheric deposition, soil water content, vertical water fluxes and exchange reactions assumed at steady-state. This procedure allows the seasonal

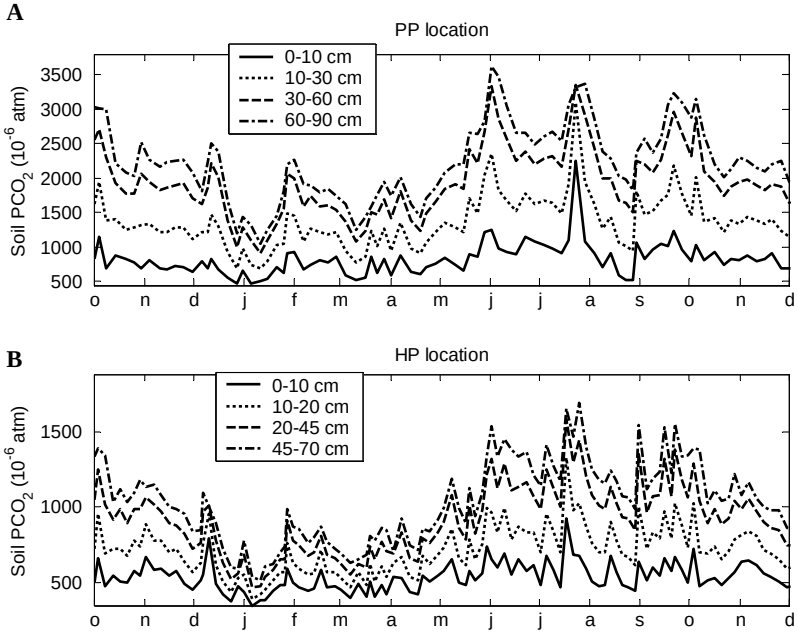

Fig. 4. Simulated soil PCO_2 by the ASPECTS model for the four top soil layers of the HP and PP locations as a function of date from October 1994 to December 1995. Below the four top layers, the PCO_2 evolution is very close to the layer 4 calculated PCO_2.

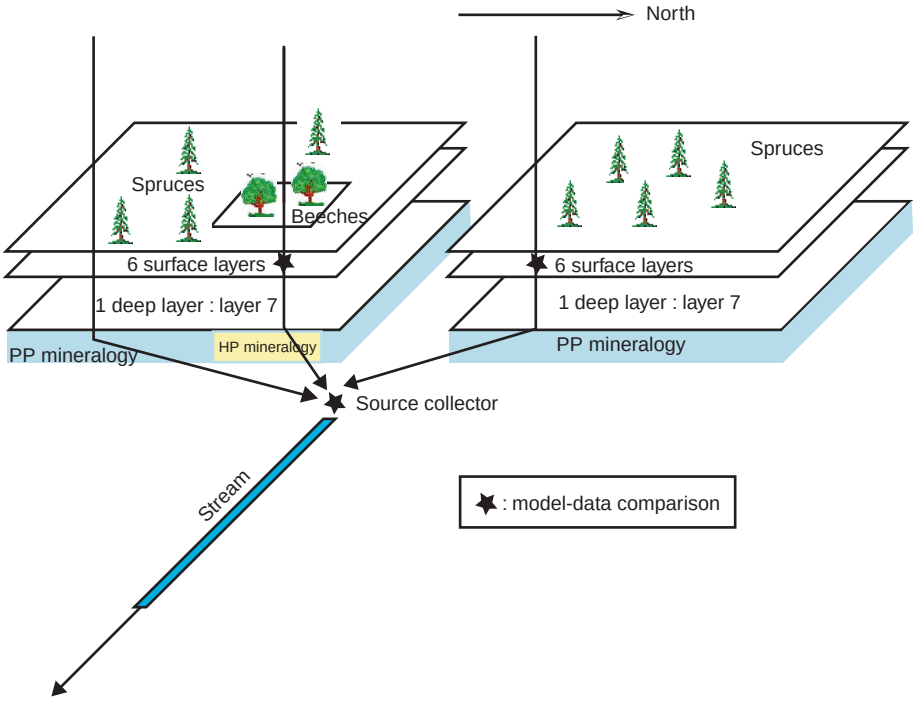

Fig. 5. The Strengbach catchment as seen by the WITCH model. The WITCH model was run for two locations (HP and PP), and results were compared with available data for the soil horizons. Then the upscaling procedure assumes that the mineralogy below the PP site (covered by spruce) can be extended to the complete area covered by the same vegetation type. The black stars stand for data-model comparison tests (at the soil level on the HP and PP location, and at the spring collector).

simulation to be started from a mean state of the system close to steady-state. However, because of the nonlinearity of the processes described within the WITCH model (including the dissolution/precipitation kinetics and exchange reactions), the mean steady-state calculated from seasonal runs differs from the steady-state calculated by mean annual runs. This required the seasonal simulations to be performed at least for several years so that initial conditions are finally relaxed. The model is run with seasonal forcing functions (temperature, soil PCO_2, water volumetric contents, vertical water fluxes, uptake and release of elements by vegetation, atmospheric deposition, all calculated by ASPECTS or measured in the field from October 1st 1994 to September 30th 1995) until steady-state is reached (achieved within 5 simulated years). These seasonal forcing functions are repeated from year to year.

A first validation of the model was performed by comparing calculated composition of soil solutions to lysimetric soil solution measurements at 10 and 70 cm (HP) and 10 and 60 cm (PP) (Fig. 5). This procedure is essentially aimed at testing the "surface" geochemical sub-model of WITCH.

3. Results of the reference simulation

3.1. Reference run, PP location

The reference run (REF simulation) was performed using the mineralogy summarized in Fig. 2, without the presence of trace minerals in the model layers. Model mean annual aqueous concentrations compare well to available data both at 10 and 60 cm, except for a slight aqueous silica overestimation at 10 cm, and a slight calcium underestimation at 60 cm depth (Figs. 6A and B). Calculated mean annual pH equals 3.91 at 10 cm depth (in agreement with the observed 4.0), and 4.84 at 60 cm depth (observed 4.4).

Mean annual SiO_2 overestimation at 10 cm essentially comes from a significant overshoot from the end of July to the end of August that is related to a sharp decrease in rainfall and vertical drainage (Fig. 7). Since almost no precipitation occurred during August 1995, modelled soil became extremely dry. Soil volumetric water content between 10 and 30 cm (layer 2) decreases from a roughly constant annual value of 0.26–0.12 m^3/m^3 in August. As a result, evapotranspiration dominates the surface hydrological budget. The vertical water flux is inverted, going from the bottom to the top, bringing up and thus concentrating aqueous SiO_2 in the top layer. The same feature is observed for all cations at 10 cm depth, in apparent disagreement with the lysimetric soil solution data. The modelled exchangeable cations are less sensitive to this hydrological event. However, lysimetric plates may not reliably capture such features occurring in extremely dry conditions, since they only collect downward water fluxes.

Apart from this discrepancy, the general seasonal behaviour at 60 cm depth is well reproduced. SiO_2, Ca^{2+} and Mg^{2+} concentrations display a general decrease from December to roughly June, and an increasing trend from

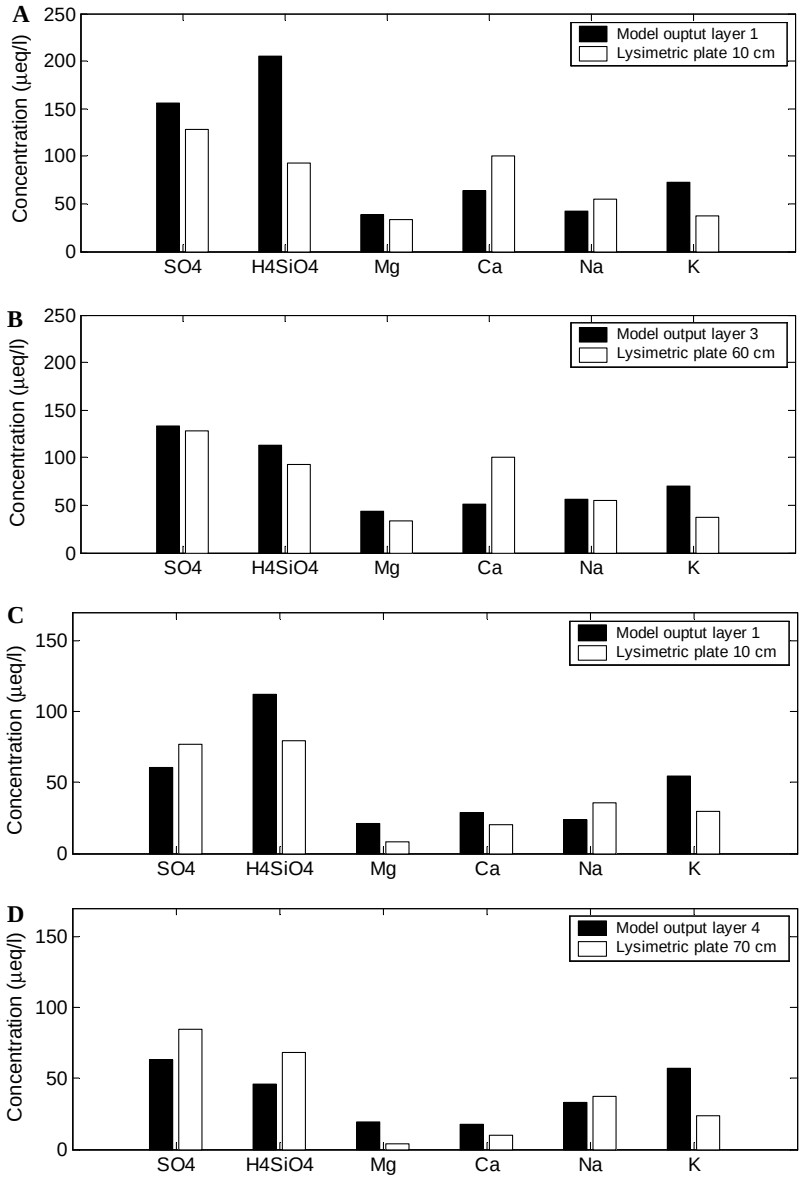

Fig. 6. Mean annual simulated concentrations (REF simulation) of sulphate (µeq/L), H_4SiO_4 (µmol/L) and major cations (µeq/L) in black, compared to the mean annual data acquired on lysimetric plates in white. (A) PP site 10 cm depth, (B) PP site 60 cm depth, (C) HP site 10 cm depth and (D) HP site 70 cm depth.

June to October (Fig. 7). Seasonal fluctuations of Na^+ concentration are not so well reproduced by the model (not shown), although the mean annual value is.

Calculated summer (mean June–July–August values) weathering profile shows that all secondary phases dissolve down to 10 cm depth, producing most of aqueous silica present in the top soil layers (Fig. 8A). Below 10 cm, Ca- and Mg-montmorillonites precipitate, while Na-montmorillonite still dissolves down to the base of the soil profile (1.8 m depth). The summer profile explains why aqueous SiO_2 accumulates in the top layer when vertical water fluxes are inverted (August 1995), since aqueous SiO_2 is then trapped within the shallow production layers (where all secondary phases dissolve).

Summer and winter (December–January–February) weathering profiles largely differ for the upper soil layers. In winter, all secondary phases dissolve down to 30 cm. Below this depth, interstitial fluids become slightly supersaturated with respect to Ca- and Mg-montmorillonites (not shown). The overall contribution of all secondary phases to the silicon budget is positive (corresponding to a dissolution) for each soil layer down to 90 cm depth, and negative below (Fig. 9A). In summer, the net silicon budget for secondary phases is positive for the top layers, but severely negative from 30 to 60 cm depth (Fig 9B). Dissolution rates of secondary minerals (expressed in kmol/m^2/s of silicon) are reduced by a factor of 1.6 in the 0–10 cm horizon in winter, compared to summer.

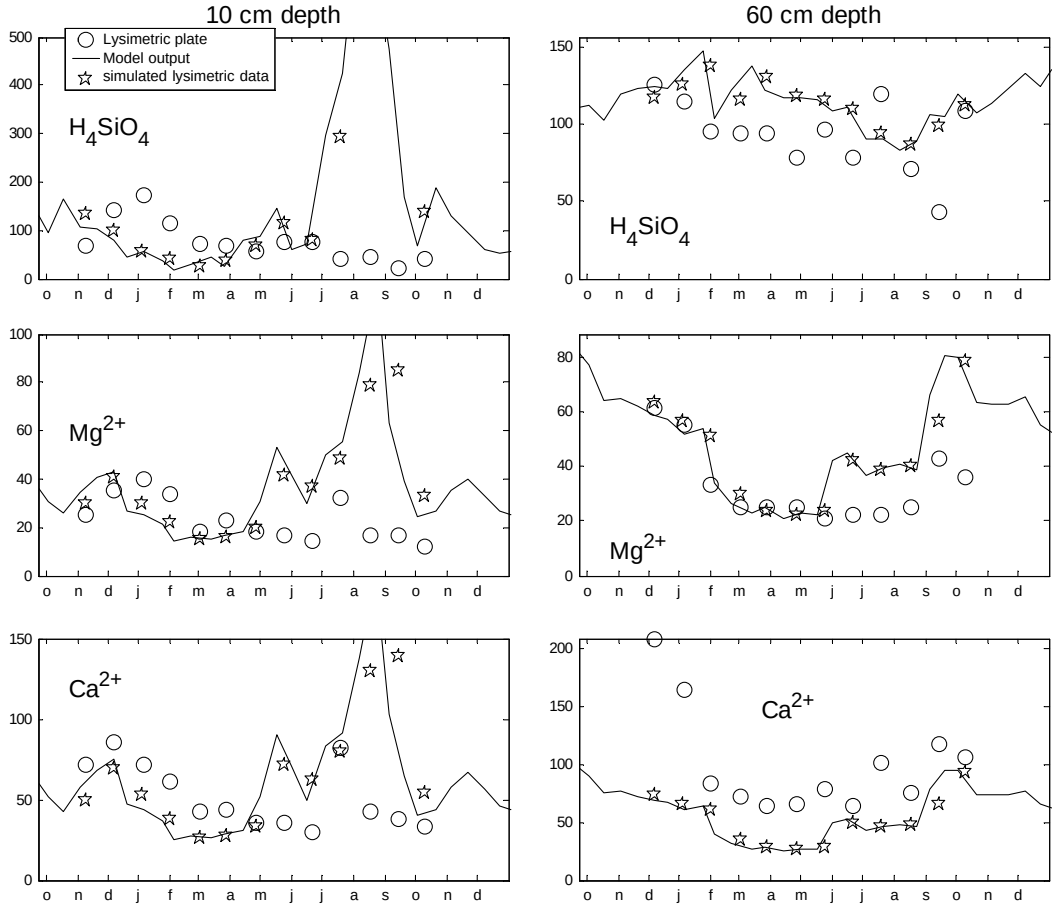

Fig. 7. Simulated H_4SiO_4, Mg^{2+} and Ca^{2+} concentration as a function of time for the PP location (REF simulation). Dots stand for data acquired on lysimetric plates, solid line is the model output, and the stars represent the simulated concentrations on lysimetric plates calculated from model output (model output are integrated over the time interval between two lysimetric plate measurements and weighted by the calculated vertical water fluxes).

The silicon budget down to 180 cm depth is largely controlled by the interaction between secondary phases and soil solutions (Figs. 9A and B). Silica release by primary mineral dissolution (mainly biotite) is only significant for the deep layer (layer 7, 1.80–10 m).

3.2. Reference run, HP location

Annual mean concentrations calculated for the HP location again roughly matches the lysimetric data (Figs. 6C and D). The main difference between model and data lies in the underestimation by the model of aqueous silica concentration at 70 cm depth. Mean annual pH is around 4.41 for the top layer (4.24 measured), and 5.35 (4.95 measured) at 70 cm depth. The August overshoot in SiO_2 at 10 cm depth is also observed although less pronounced (Fig. 10). Exchangeable cations do not show any simultaneous peak. The main reason for this divergence is the difference in the standing vegetation from PP to HP. Evapotranspiration appears to be less important during dry months for beeches located on the more humid North slope than for spruces.

The model roughly matches the measured seasonal fluctuations for Mg^{2+}, Ca^{2+} and SiO_2 (particularly at 10 cm depth, and except for the August overshoot), although it slightly overestimates Ca^{2+} and Mg^{2+} concentrations (Fig. 10). Mg^{2+} concentration overestimation is essentially linked to higher Mg^{2+} concentration in throughfall (mean 11 μeq/L) than in measured soil solutions (8 μeq/L), and possibly to overevaluated dissolution of smectites in the upper soil layer. Interestingly, calculated Na^+ concentration at 10 cm is dephased by about 6 months compared to the data, a feature mainly driven by the throughfall Na^+ input. Mg^{2+}, Na^+ and Ca^{2+} seasonal fluctuations roughly follow measurements at 70 cm depth (Fig. 10).

Summer and winter weathering profiles differ for the top soil layers (not shown). In winter, all secondary phases dissolve down to 30 cm. Below this depth, precipitation of Ca-, K- and Mg-montmorillonites occurs. In summer, all montmorillonites precipitate below 10 cm except Na- and K-montmorillonites. Furthermore, weathering rates of secondary minerals (expressed in kmol/m^2/s of silicon) are reduced by a factor of 2 in the 0–10 cm horizon in winter, compared to summer. Silicon budget down to 150 cm depth is largely controlled by the interaction between secondary phases and soil solution (Figs. 9C and D). For the deep layer (layer 7, 1.50–10 m), both primary and secondary mineral dissolutions (mainly biotite and albite)

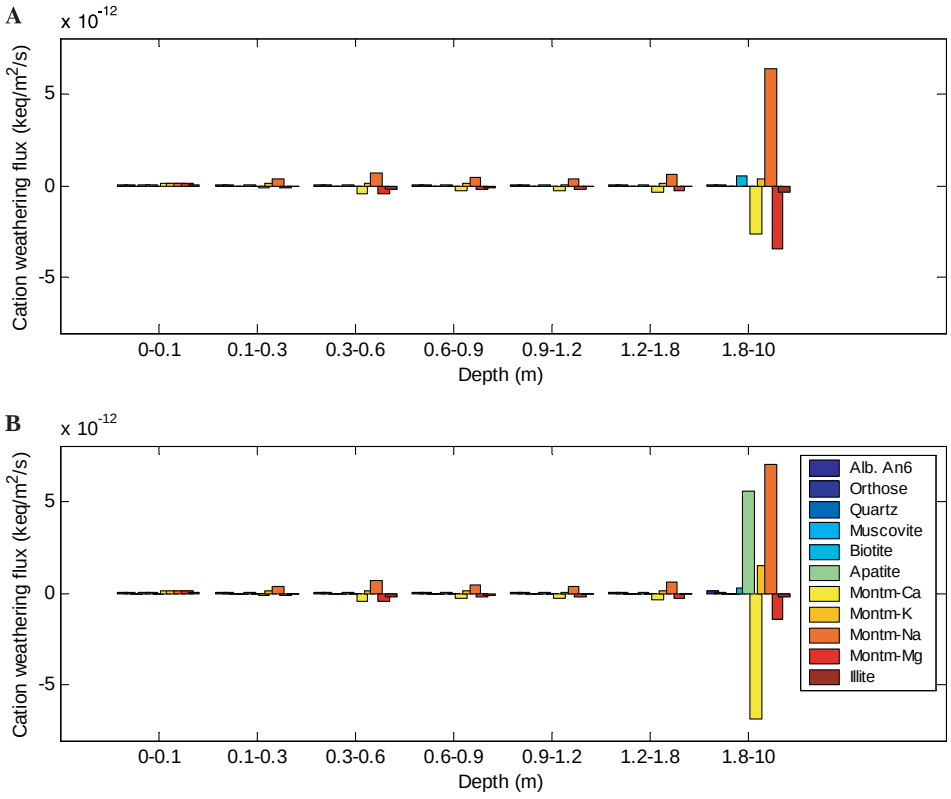

Fig. 8. Calculated base cation flux through weathering or precipitation as a function of the model layer (PP location), and of the minerals, in keq of cations per m^2 per second. (A) REF simulation, without apatite, (B) APL10 simulation with apatite only added to the deepest layer at 10% of the measured abundance in the unaltered rock. All plotted results are for the summer (mean value covering the June–July–August period).

release Si at depth during summer, resulting in a net release of 13.4×10^{-13} kmol of Si/m^2/s, while secondary phase precipitation almost balance the Si release by primary mineral dissolution in winter.

3.3. Calculating the chemical composition of the main stream at the spring collector

The WITCH model appears to be able to simulate the concentration of the main species within the soil horizons down to about 70 cm depth, a conclusion already reached with the SAFE model for mean annual simulations (Sverdrup and Warfinge, 1995; Alveteg, 1998; Sverdrup et al., 2002) mainly for Sweden sites. Furthermore, the model also captures first-order seasonal fluctuations for several major species, although discrepancies are sometimes observed. The next challenge now is to check whether the WITCH model can capture the chemical composition of the main stream, through the mixing of the two defined end-members (HP and PP locations). The upscaling of a weathering model working at the soil scale to the watershed scale is a perilous operation. One way of proceeding would be to force the WITCH model with a full 3D physical hydrological model. Such model would require far too many boundary conditions unconstrainable by measurements. As a first attempt towards an integrated modelling of weathering processes at the catchment scale using laboratory kinetic laws for the dissolution/precipitation of minerals, we choose a quite simple procedure: the results obtained on the PP location are extended to 80% of the total surface of the catchment (equivalent to the surface covered by spruces), while results obtained for the HP location are extended to the 20% of the area covered by beeches. This procedure allows to account for the differences in soil weathering processes related to standing vegetation type, since we found that most of the geochemical signature of the percolating waters are controlled by the interactions between soil solutions and secondary minerals. Such interactions are most probably largely dependent on the hydrological behaviour of the soil profile, itself directly related to the standing vegetation type. But this procedure neglects the variability in mineralogical composition of the bedrock inside the area covered by a given vegetation type (see discussion about the Ca^{2+} budget in Section 7). Furthermore, at this point of the model development, we were not able to account for lateral transfers of water, or for respective influence of particular contributive areas such as the saturated area connected to the stream (Idir et al., 1999) which vary according to hydrological conditions. We assume that the main stream is fed throughout the year with waters percolating down to the deepest layer, then reaching the impermeable bedrock and flowing to the main stream. As a result, concentrations in the main stream Q_{stream} are calculated as follows:

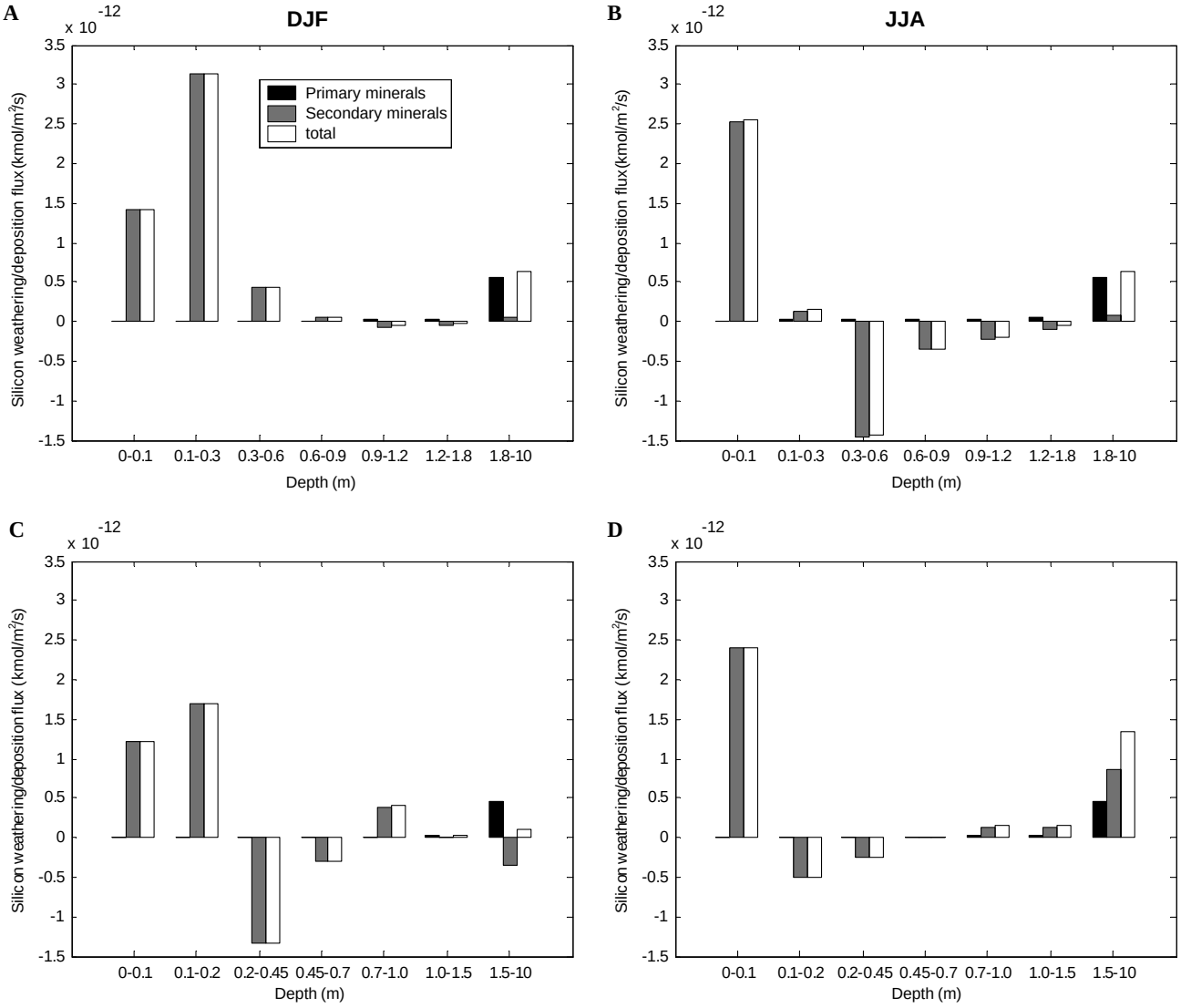

Fig. 9. Simulated exchange of Si between soil solutions and minerals at various depth for the REF simulation. A negative value corresponds to a removal of Si through secondary mineral precipitation, while a positive value stands for an input into the soil solution through a dissolution process. (A) PP location, winter (December–January–February). (B) PP location summer (June–July–August). (C) HP location winter. (D) HP location summer. Note that the scale is not the same from one plot to the other.

$$Q_{\text{stream}} = 0.80 \cdot Q_{\text{PP}} + 0.20 \cdot Q_{\text{HP}}, \quad (5)$$

where Q_{HP} and Q_{PP} represents, respectively, the concentrations of the various chemical species of interest within layer 7 for the HP and PP locations. This mixing is performed at a seasonal scale, but at this stage, results will be only presented on a mean annual basis since the assumption that all contributing waters are percolating down to the bedrock is justified only at the mean annual scale. All model outputs are now compared to data acquired at the spring collector.

The results yielded by the reference simulation for the spring collector differ significantly from the data. In particular, Na^+ concentration is overestimated by a factor of 1.7, while Ca^{2+} and Mg^{2+} are underestimated. The biggest discrepancy, however, is observed for Ca^{2+}. The model predicts a mean annual Ca^{2+} concentration at the spring collector of 13.5 μeq/L, compared to the observed 158 μeql/L (Fig. 11). On the other hand, aqueous silica is accurately predicted by the model (130 μmol/L calculated vs 140 μmol/L measured).

Mg^{2+} underestimation can be easily understood considering the integrated silica budget through the soil horizons. Soil solutions become supersaturated with respect to smectite minerals with increased depth (except Na-montmorillonite), resulting in the removal of Mg^{2+} and silica from the soil solutions during their downward percolation. On the other hand, Na^+ overestimation results from the dissolution of Na-montmorillonite throughout all horizons in winter and summer. This dissolution of Na-montmorillonite supplies enough aqueous silica, compensating for the removal through Ca- and Mg-montmorillonite precipitation, explaining why the silica flux is correctly estimated, while the Mg^{2+} flux is not.

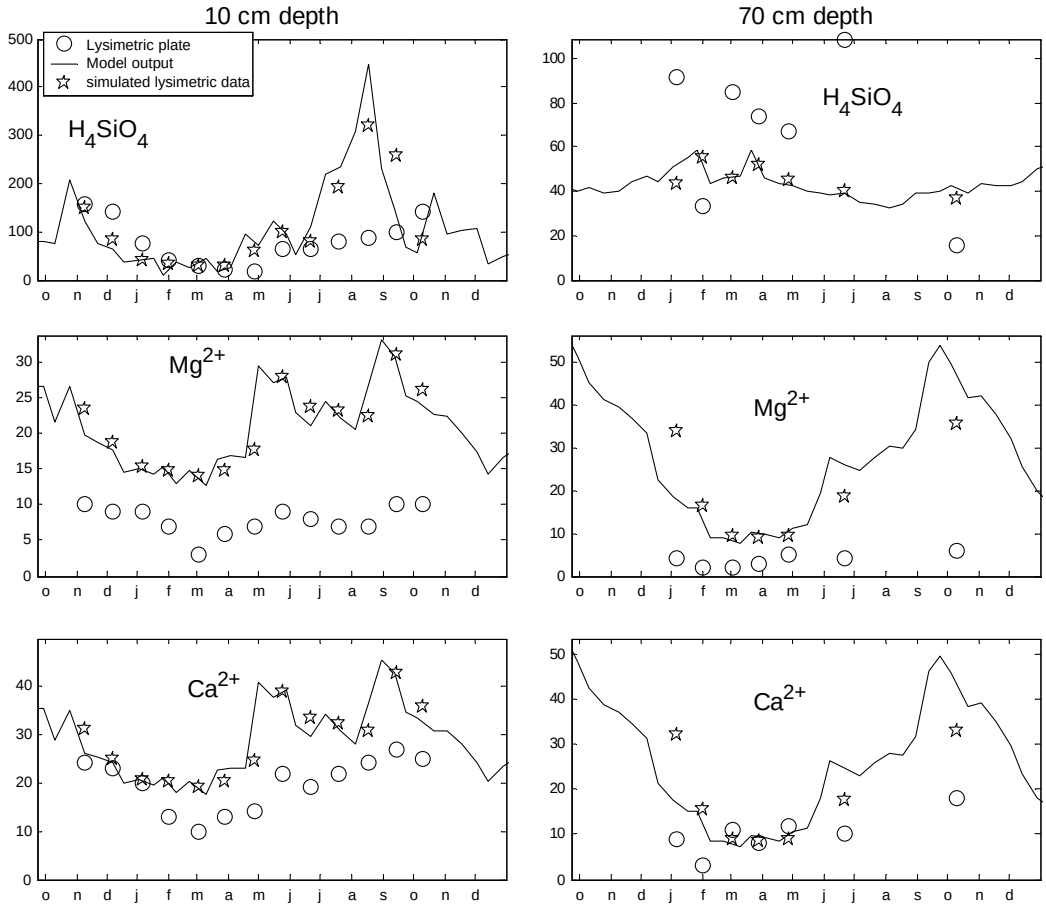

Fig. 10. Simulated H_4SiO_4, Mg^{2+} and Ca^{2+} concentration as a function of time for the HP location (REF simulation). Dots stand for data acquired on lysimetric plates, solid line is the model output, and the stars represent the simulated concentrations on lysimetric plates calculated from model output (model output are integrated over the time interval between two lysimetric plate measurements and weighted by the calculated vertical water fluxes).

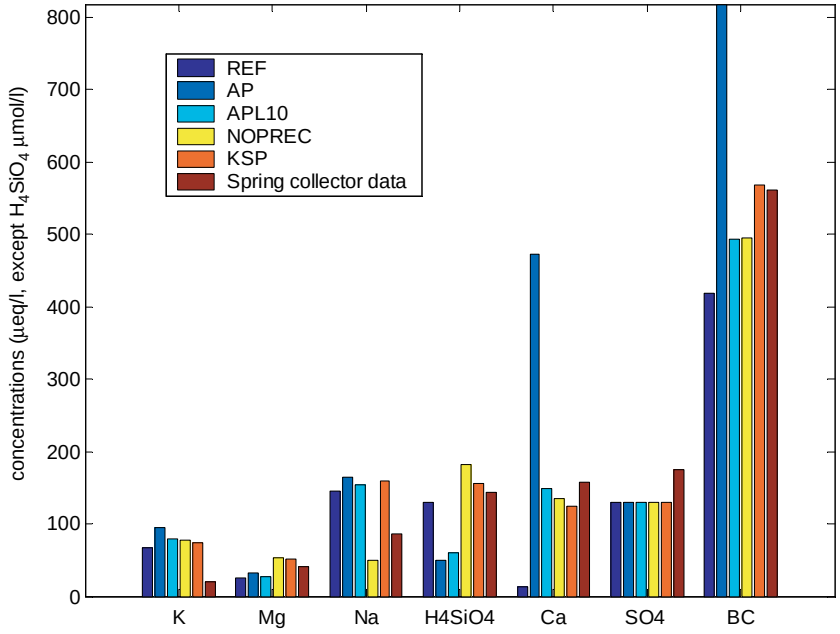

Fig. 11. Mean annual calculated concentrations of major cations, H_4SiO_4 and sulphate at the spring collector, compared to spring collector data, and for the reference and sensitivity tests performed (see description in the text).

4. AP and APL10 sensitivity tests: Looking for calcium at the spring collector

The lack of Ca^{2+} in the calculated chemical composition at the spring collector suggests us a first sensitivity test (AP simulation, Table 4), where apatite is added in each layer as a trace mineral based on the mineralogical composition determined by Fichter et al. (1998a) (for HP: 0.2% vol of apatite down to 70 cm depth, 0.3% vol below; for PP: 0.1% vol down to 30 cm depth, 0.3 between 30 and 90 cm depth, 0.8% vol below). Results at the spring collector show large changes in the calculated abundance of major elements (Fig. 11), as well as the concentrations of Ca^{2+} and SiO_2 in the soil solutions above 60–70 cm. In soil profiles, Ca^{2+} increases significantly while SiO_2 concentrations falls by a factor of about 2.2 at 60–70 cm depth (PP profile). Ca^{2+} increases are driven by the massive release of Ca^{2+} through apatite dissolution in all layers (peaking at 1×10^{-11} keq/m^2/s in the top soil horizon in summer, under strongly acidic conditions, compared, for instance, to biotite dissolution reaching a weak 2×10^{-14} keq/mol/m^2 within the same soil horizon). The silica depletion in soil solution is driven by the abundant Ca-montmorillonite precipitation, itself driven by the important Ca^{2+} concentration increase. The link between the presence of trace apatite and secondary phase precipitation is particularly visible in the deepest model layer: Ca-montmorillonite precipitation removes up to 8×10^{-12} keq/m^2/s of base cations (mean June–July–August) in the AP simulation, compared to the 2.5×10^{-12} keq/m^2/s in the REF simulation. The model yields similar results for the HP location.

As a direct consequence of the introduction of trace apatite in the soil horizons, calculated annual mean Ca^{2+} concentrations at the spring collector reaches 470 μeq/L, compared to the measured 158 μeq/L (reference simulation yielded 13.5 μeq/L, Fig. 11). Furthermore, the enhanced precipitation of Ca-smectites within the soil horizons and in the deepest layer result in a sharp decrease of the calculated Si concentration at the spring collector (Si concentration falls down to 50 μmol/L, compared to the observed 140 μmol/L and simulated 130 μmol/L in the reference run).

Table 4
Sensitivity simulations

	Apatite (% vol in each layer)	Secondary mineral precipitation
REF	No HP: 0-0-0-0-0-0-0 PP: 0-0-0-0-0-0-0	Yes
AP	Yes in all layers HP: 0.2-0.2-0.2-0.2-0.3-0.3-0.3 PP: 0.1-0.1-0.3-0.3-0.8-0.8-0.8	Yes
APL10	Yes in deepest layer only HP: 0-0-0-0-0-0-0.03 PP: 0-0-0-0-0-0-0.08	Yes
NOPREC	Yes in deepest layer HP: 0-0-0-0-0-0-0.03 PP: 0-0-0-0-0-0-0.08	No
KSP	Yes in deepest layer HP: 0-0-0-0-0-0-0.03 PP: 0-0-0-0-0-0-0.08	Yes (montmorillonite solubility products multiplied by 8)

The presence of apatite within the top soil horizons might be questionable. Apatite dissolution rate is so fast (4 orders of magnitude faster than of plagioclase (An_6) dissolution) that this mineral is not likely to be preserved in highly altered horizons. Indeed, apatite was found in the upper horizons, but mainly as inclusions within much less reactive minerals such as quartz (Fichter et al., 1998b). Hence, in spite of a high solubility, apatite is not available for dissolution in the upper soil layers (El Gh'Mari, 1995; Fichter et al., 1998a; Probst et al., 2000), and its contribution to Ca budget in surface horizons is suspected to be low (Aubert, 2001).

For that reason, we performed a second sensitivity test (APL10 simulation) assuming the dissolution of apatite only within deep layer 7, with the abundance estimated by (Fichter et al., 1998a) (0.8% in volume for PP, 0.3% in volume for HP) reduced by a factor of 10 (new abundance of 0.08% for PP, and 0.03% for HP). This 10% factor corresponds to the best fit of the Ca^{2+} data at the spring collector by the model. The introduction of the 10% factor can be justified by the fact that bedrock surface in contact with reacting solution is likely to be strongly depleted in apatite because of the very high dissolution rate of this mineral compared to silicate phases. Furthermore, the APL10 simulation yields exactly the same results as the reference simulation for the soil layers down to 150/180 cm depth, where the agreement between data and model results was quite good. The Ca^{2+} concentration calculated at the spring collector declines from 510 μeq/L (AP simulation) down to 150 μeq/L, matching the observed 158 μeq/L (Fig. 11). However, the APL10 simulation does not yield significant increase in calculated aqueous silica concentration compared to the AP simulation. It remains too low compared to the data, suggesting that the extent of well crystallized clay precipitation is overestimated, and mainly amorphous and poorly crystalline phases probably form instead.

5. NOPREC and KSP simulation: Looking for silica at the spring collector (Table 4)

The two critical factors when trying to fit the spring collector data appear to be the abundance of apatite within the soil horizons, and the amount of precipitated secondary minerals. The extent of secondary silicate precipitation depends on the solubility products of the crystallizing phases and their precipitation kinetics. Both are important sources of uncertainties, but the computation of true chemical equilibrium with precipitating solids is particularly crucial since available thermodynamic databases only refer to well crystallized clay minerals, and not to poorly crystallized and amorphous silicates that are largely found to precipi-

tate during low temperature chemical weathering (White and Blum, 1995; Stefansson and Gislason, 2001).

The calculated depletion in silica at the spring collector result from the abundant precipitation of secondary silicates. The NOPREC test was performed by assuming the presence of trace apatite in the deepest layer at 10% of the fresh rock abundance and by impeding the precipitation of secondary silicates. When supersaturation is reached with respect to kaolinite, montmorillonites or illite, the dissolution and precipitation rates of these secondary minerals are set to zero. It can be seen on Fig. 11 that, for this test, aqueous silica concentration rises at the spring collector, reaching 181 μmol/L (mean annual concentration), slightly above the observed 140 μmol/L. Mg^{2+} concentration also increases (54 μeq/L calculated, 40 observed, 26 in APL10 test), while Na is reduced by a factor 3 (50 μeq/L).

Preventing precipitation of secondary phases is an extreme test. A last sensitivity test (KSP) was performed by artificially increasing the solubility product of well-crystallized smectites (the dominant secondary phase in the Strengbach catchment in terms of silica budget), to account for the fact that these secondary phases are probably poorly crystallized. As in the APL10 and NOPREC simulations, apatite abundance was fixed at 10% of the fresh rock abundance in the lowest layer. Several values of the solubility products of smectites were tested and the best fit is obtained when these solubility products are increased by a factor of 8. Aqueous silica, Mg^{2+} and Ca^{2+} concentration all fit the available data at the spring collector, while the results in the soil profile above 70 cm remains qualitatively unchanged compared to the reference simulations (except for a general slight increase in Si concentration at 60 cm (PP) and 70 cm (HP) depth in summer). As a consequence, the total base cation concentration (and hence the atmospheric CO_2 consumption through rock weathering once SO_4^{2-} contribution is removed) at the spring collector is correctly predicted by the model (569 μeq/L compared to the observed 560 μeq/L).

6. Trace mineral and base cation budget of a granitic catchment

The contribution of trace minerals (including epidote, apatite, calcite) to the production of base cations during weathering in various granitic catchments has been investigated through $^{87}Sr/^{86}Sr$ measurements of soil solutions and stream waters (Clow et al., 1997; Aubert et al., 2001, 2002; Blum et al., 2002; Oliva et al., 2004; White et al., 2005a). As shown in Table 5, these estimations span a large range of values. For the Strengbach catchment, the WITCH model gives a value of 60% of base cations released through weathering of trace apatite at the spring collector (KSP simulation, representing the best fit of the spring collector data), a value higher than the 15% estimated by (Aubert et al., 2001). However, this high calculated value is mainly driven by the contribution from the PP location where apatite contribution to base cation flux reaches 69%. This value reflects the hydrothermally altered mineralogy of the PP site where apatite abundance reaches 0.8%. This mineralogy was extended to 80% of the watershed area through our upscaling procedure based on vegetation type abundance. For the HP location, the model yields only 26% of base cation originating from apatite dissolution, a value closer to the (Aubert et al., 2001) estimation, and the HP mineralogy is probably more representative of the mean catchment mineralogy (El Gh'Mari, 1995). On the other hand, $^{87}Sr/^{86}Sr$ mixing models may yield large uncertainties, especially when the contribution of apatite is potentially important.

7. Some uncertainties and limitations

We deliberately focused on the Ca^{2+}, Mg^{2+} and aqueous silica concentration, in our attempt to validate the WITCH model at the spring collector. However, it is worthy to look at the Na^+ and K^+ behaviour in the various simulations. Considering the concentrations calculated at the spring collector (Fig. 11), Na^+ displays a rather conservative behaviour from one simulation to the other (except NOPREC), with a calculated concentration overestimated at about 150 μeq/L compared to the observed 85 μeq/L. The main source of Na^+ within the various layers is the dissolution of Na-montmorillonite that is unstable in all simulations but the NOPREC one. Indeed, Na^+ concentration falls to 49 μeq/L in the NOPREC simulation. Because precipitation of all secondary phases are inhibited, pH rises within all layers, and with increasing depth soil solutions become supersaturated with respect to Na-montmorillonite. For instance, pH rises from 4.86 in the APL10 run (in summer, PP location) to 5.43 in the NOPREC simulation in soil layer 3 (30–60 cm depth), resulting in a strong decrease of Na^+ release within the soil layers.

Table 5
Contribution of trace minerals to the total base cation flux exported from the watershed

	Main stream BC flux (weathering contribution only) (meq/m^2/year)	Percentage of the Ca flux originating from trace mineral dissolution relative to the total BC flux
Hubbard Br.	101 (Drever and Clow, 1995)	23.5% (trace apatite) (Blum et al., 2002)
Estibère	167 (Oliva et al., 2004)	80% (trace silicates) (Oliva et al., 2004)
Loch Vale	42 (Mast et al., 1990)	41% (trace calcite) (Clow et al., 1997; White et al., 1999)
Strengbach	Measured: 281	15% (trace apatite) (Aubert et al., 2001)
	KSP simulation (spring collector): 285	26% (HP) to 69% (PP) (trace apatite) (This study)

K^+ is not sensitive to the inhibition of secondary phases precipitation and stabilizes around 70 μeq/L in all simulations (Fig. 11), a value close to the mean 62 μeq/L measured in throughfall, which was used as the input of K^+ at the surface. The overestimation of K^+ concentration at the spring collector is most probably linked to an underestimation of the cycling of K^+ within the top soil layers. Potassium is extremely sensitive to the biological activity in soils (White et al., 2005b). In this study, the uptake of K^+ by standing vegetation is calculated from the uptake of carbon in each soil layers by the ASPECTS model, a process that extends down to 0.9 m depth. It is possible that K^+ uptake occurs mainly at a shallower depth, preventing this cation from percolating down to the bedrock and to concentrate in the spring collector.

Another possible source of error comes from the assumption that the four types of montmorillonite (Ca-, Na-, K- and Mg-) are equally abundant in each soil layers. This assumption was made since only the total abundance of smectites was measured. For instance, assuming the absence of Mg-montmorillonite within the smectite pole leads to a 3.5 times decrease in the calculated Mg^{2+} concentration at the spring collector. Aqueous silica, Na^+ and K^+ remain almost unchanged, but Ca^{2+} concentration is multiplied by 1.5.

We also test the impact of changing illite solubility product on the cation and aqueous silica concentrations at the spring collector. Decreasing by a factor of 10 this solubility product does not significantly modify the results at the spring collector. Smectites are clearly the dominant secondary phases in terms of dissolved load of the waters.

Thermodynamic data selection appears critical since precipitation of secondary silicate phases exerts a major control on cation and SiO_2 export at the watershed scale. Available thermodynamic databases are not fully compatible and coherent. In this work, we took a special care at calculating the solubility product of minerals from the most coherent and robust values for the ΔG_f^0 of reacting aqueous species and solids. Similar efforts were devoted to the calculation of the enthalpies of mineral dissolution reaction ΔH_r^0 from the ΔH_f^0 of reacting species. Despite this special care, significant uncertainties affect the thermodynamic properties of clay minerals, particularly smectites, which control the precipitation of secondary phases. In this study, the Gibbs free energies of all montmorillonites were taken from the most recent SUPCRT values (file speq03. dat). ΔG_f^0 values listed in SUPCRT refer to idealized montmorillonites and have been estimated using the "linear approach" of Tardy and Garrels (1974) that assumes that the Gibbs energy of a sheet silicate is the sum of the Gibbs energies of a collection of "silicated" oxide and hydroxide components. Regarding aqueous species, the main uncertainties and controversies affect aluminium and aqueous silica. Thermodynamic properties of Al^{3+} and Al hydrolised species were taken from Wesolowski and Palmer (1994) and Castet et al. (1993) which are in good agreement and have been demonstrated to be the most reliable (Tagirov and Schott, 2001). Accordingly, $\log K$ values for all Al-bearing minerals were calculated using these data. For aqueous silica, calculations were performed using the value determined by Walther and Hegelson (1977). However, a new value has been recently proposed by Rimstidt (1997) and incorporated in SUPCRT that is 350 cal/mol more negative than the former value ($\Delta G^0_{f_{(298.15)}} = -199.54$ kcal/mol). This revised free energy of SiO_2(aq) yields a significant increase of the solubility product of silicate phases. For example, the solubility product of montmorillonites at 25 °C is increased by about one order of magnitude. The impact of this new value on calculated results was tested by performing again the APL10 simulation that assumes the dissolution of apatite only within deep layer 7, with a volumetric abundance ten times below the fresh rock measured abundance. The model predicts correct Ca^{2+} and Mg^{2+} concentrations at the spring collector (not shown), but aqueous silica concentration remains underestimated (calculated concentration at 90 μmol/L). Once again, the same discussion about precipitation of well crystallized phases apply, and the solubility products of montmorillonite must be artificially increased to account both for the base cation and aqueous silica concentration at the spring collector, in agreement with the conclusions reach above.

Accurate prediction of secondary minerals precipitation rates is a major challenge due to the paucity of experimental data, unlike for dissolution rates. In this study precipitation rates were described within the framework of the TST by applying the principle of detailed balancing to the overall reaction (Eq. (3)). s, the order of the dependence of precipitation rate on the saturation index, was set equal to unity since it is difficult to predict it a priori. However, simulation tests performed with different s values demonstrated that $s \ll 1$ induced strong solution supersaturations and thus affected calculated concentrations at the collector.

8. Conclusions

This contribution was aimed at constructing a numerical model of weathering at the catchment scale: the WITCH model. The model mainly relies on laboratory kinetic laws to describe chemical weathering in the natural environment. For the first time, a weathering model was forced on a seasonal basis with output of a biospheric productivity model to constrain soil CO_2 levels, and release/uptake of elements by the vegetation. Furthermore, the model operation was extended from the root zone down to the bedrock (10 m depth) through the addition of a deep layer with a long residence time (8 months) to account for weathering processes at depth. WITCH was used to simulate weathering processes in soil profile and at the catchment scale for the Strengbach (Vosges) small granitic watershed in temperate environment. The simulations yield the following conclusions:

(1) We first validate the chemical module of the WITCH model for two soil profiles of the Strengbach catchment, and show that the model is able to reproduce the general behaviour of most major species on a mean annual basis down to 70 cm depth in the soil, and without considering the presence of any trace minerals. As previously stated (Sverdrup et al., 2002), kinetic laws are able to describe weathering processes within soil horizons, as long as the inhibiting effect of aqueous species on mineral dissolution and the affinities of involved chemical reactions are taken into account. Furthermore, WITCH is able to roughly reproduce the seasonal fluctuations of Ca^{2+}, Mg^{2+} and Si concentrations in interstitial solutions of Strengbach soils.

(2) The silicon budget is almost totally controlled by precipitation/dissolution of secondary minerals (here montmorillonite) inside the root zone. Dissolution of primary minerals contribute marginally to the silicon and cation budget within the root zone.

(3) When simulating the chemical composition at a spring collector through simple integration of the results obtained at the soil profile scale, WITCH was not able to reproduce the observed Mg^{2+} and Ca^{2+} concentrations on annual basis. The calculated depletion in silica and Mg^{2+} (2–3 times lower than measurements) is linked to an ample precipitation of well crystallized secondary phases (smectites) integrated from the surface down to the bedrock. The most dramatic discrepancy between model result and data affects Ca^{2+} concentrations (underestimated by a factor of 10). This last result suggests a peculiar origin for Ca^{2+} at the spring collector and in the main stream.

(4) Adding (in agreement with reported bedrock and soil mineralogical composition) trace apatite within the various soil horizon and in the deep box yields a tremendous increase in calculated Ca^{2+} concentration at the spring collector, with a subsequent removal of aqueous SiO_2 through precipitation of secondary minerals triggered by the massive release of Ca^{2+} within all model layers. This leads to a strong decrease in the concentration of aqueous silica at the spring collector (50 μmol/L compared to the measured 140 μmol/L). The model yields thus only 35% of the observed Si concentration at the spring. Assuming the presence of trace apatite only in the deepest layer (below 1.50 m) with an abundance ten times below the observed abundance in fresh granitic rocks allows the calculation of a Ca^{2+} concentration at the spring collector in agreement with available data. However, a strong deficit in aqueous silica is still calculated. Preventing precipitation of well crystallized clay minerals erases the deficit in aqueous silica, suggesting that poorly crystallized, amorphous phases should be included into weathering models. As an illustration, increasing the solubility product of all smectites by a factor of 8 yields an accurate prediction of Mg^{2+}, Si and Ca^{2+} concentrations at the spring collector.

(5) Rigorous modeling of secondary mineral precipitation is essential to decipher the main sources and mechanisms controlling the release of chemical species, to predict their fluxes and thus subsequent atmospheric CO_2 consumption. This requires not only reliable data on the rate of precipitation of clay minerals but also knowledge of the solubility products of the poorly crystalline solid phases likely to form in soils. Moreover, approximation of nucleation rates would be necessary for predicting the precipitation of minerals not present in the soil.

Acknowledgments

Mattias Alveteg and Harald Sverdrup at Lund University are greatly acknowledged for helpful discussions, and help in the computing of exchange processes. A. Clement and B. Fritz at the CGS in Strasbourg helped us with valuable advices when this project was settled. We thank Jean Riotte, Bernard Dupré, Gilles Berger, Oleg Pokrovsky, Eric Oelkers, Jean-Louis Dandurand at LMTG for fruitful discussions. Tom Wolery at Lawrence Livermore Lab is thanked for providing the last SUPCRT versions and for invaluable informations on the origin of montmorillonite thermodynamic data listed in SUPCRT databank. PRAKSYS is acknowledged for the maintenance of the cluster of PC at LMTG, on which simulations have been performed. L.M. François is Research Associate at the Belgian National Foundation for Scientific Research (FRNS). The EGIDE/TOURNESOL program partly financed this work. Tim Drever, Harald Sverdrup and an anonymous reviewer are greatly acknowledged for their careful and constructive reviews, that contribute to improve the original manuscript.

Associate editor: Dimitri A. Sverjensky

References

Alveteg, M., 1998. Dynamics of forest soil chemistry. Ph.D, Lund University.

Amiotte-Suchet, P., Probst, J.L., Ludwig, W., 2003. World wide distribution of continental rock lithology: implications for atmospheric/soil CO_2 uptake by continental weathering and alkalinity river transport to the oceans. *Global Biogeochem. Cycles* **17** (2).

Aubert, D., 2001. Contribution de l'altération et des apports atmosphériques aux transferts de matières en milieu silicaté: traçage par le strontium et le terres rares. Cas du bassin versant du Strengbach (Vosges, France). Ph.D, Université Louis Pasteur.

Aubert, D., Probst, A., Stille, P., Viville, D., 2002. Evidence of hydrological control of Sr behavior in stream water (Strengbach catchment, Vosges mountains, France). *App. Geochem.* **17**, 285–300.

Aubert, D., Stille, P., Probst, A., 2001. REE fractionation during granite weathering and removal by waters and suspended loads: Sr and Nd isotopic evidence. *Geochim. Cosmochim. Acta* **65**, 387–406.

Aumont, O., Orr, J.C., Monfray, P., Ludwig, W., Amiotte-Suchet, P., Probst, J.L., 2001. Riverine-driven interhemispheric transport of carbon. *Global Biogeochem. Cycles* **15** (2), 393–405.

Berner, R.A., Kothavala, Z., 2001. GEOCARB III: a revised model of atmospheric CO_2 over Phanerozoic time. *Am. J. Sci.* **301**, 182–204.

Blum, A.E., Stillings, L.L., 1995. Feldspar dissolution kinetics. In: White, A.F., Brantley, S.L. (Eds.), *Chemical Weathering Rates of Silicate Minerals, Reviews in Mineralogy*, Vol. 31, pp. 291–351.

Blum, J.D., Klaue, A., Nezat, C.A., Driscoll, C.T., Johnson, C.E., Siccama, T.G., Eagar, C., Fahey, T.J., Likens, G.E., 2002. Micorrhizal weathering of apatite as an important calcium source in base-poor forest ecosystems. *Nature* **417**, 729–731.

Bonhomme, M., 1967. Ages radiométriques de quelques granites des Vosges moyennes. *Bull. Carte géol. Als. Lorr.* **20**, 101–106.

Brady, P.V., Carroll, S.A., 1994. Direct effects of CO_2 and temperature on silicate weathering: possible implications for climate control. *Geochim. Cosmochim. Acta* **58** (8), 1853–1856.

Castet, S., Dandurand, J.-L., Schott, J., Gout, R., 1993. Boehmite solubility and aqueous aluminum speciation in hydrothermal solutions (90–350 °C): experimental study and modeling. *Geochim. Cosmochim. Acta* **57**, 4869–4884.

Chaïrat, C., 2005. Etude expérimentale de la cinétique et des mécanismes d'altération de minéraux apatitiques: Application au comportement d'une céramique de confinement d'actinides mineurs. Ph.D thesis, Université Paul Sabatier, Toulouse.

Clow, D.W., Mast, M.A., Bullen, T.D., Turk, J.T., 1997. 87Sr/86Sr as a tracer of mineral weathering reactions and calcium sources in an alpine/subalpine watershed, Loch Vale, Colorado. *Water Resour. Res.* **33**, 1335–1351.

Dambrine, E., Sverdrup, H., Warfinge, P., 1995. Atmospheric deposition, forest management and soil nutrient availability: a modelling exercise. In: Landmann, G., Bonneau, M. (Eds.), *Forest decline and atmospheric deposition effects in the French mountains*. Springer-Verlag, New York.

De Pury, D.G.G., Farquhar, G.D., 1997. Simple scaling of photosynthesis from leaves to canopies without errors of big-leaf model. *Plant, Cell Environ.* **20**, 537–557.

Dessert, C., Dupré, B., François, L.M., Schott, J., Gaillardet, J., Chakrapani, G.J., Bajpai, S., 2001. Erosion of Deccan Traps determined by river geochemistry: impact on the global climate and the $^{87}Sr/^{86}Sr$ ratio of seawater. *Earth Planet. Sci. Lett.* **188** (3/4), 459–474.

Dessert, C., Dupré, B., Gaillardet, J., François, L.M., Allègre, C.J., 2003. Basalt weathering laws and the impact of basalt weathering on the global carbon cycle. *Chem. Geol.* **202**, 257–273.

Devidal, J.L., Schott, J., Dandurand, J.-L., 1997. An experimental study of kaolinite dissolution and precipitation kinetics as a function of chemical affinity and solution composition at 150 °C, 40 bars, and pH 2, 6.8, and 7.8. *Geochim. Cosmochim. Acta* **61**, 5165–5186.

Donnadieu, Y., Goddéris, Y., Ramstein, G., Nédelec, A., Meert, J.G., 2004. Snowball Earth triggered by continental break-up through changes in runoff. *Nature* **428**, 303–306.

Dove, P.M., 1994. The dissolution kinetics of quartz in sodium chloride solutions at 25 ° to 300 °. *Am. J. Sci.* **294**, 665–712.

Drever, J.I., 1997. The Geochemistry of Natural Waters. Prentice Hall, Upper Saddle River, New Jersey 07458.

Drever, J.I., Clow, D.W., 1995. Weathering rates in catchments. In: White, A.F., Brantley, S.L. (Eds.), *Chemical Weathering Rates of Silicate minerals*, Vol. 31. Mineralogical Society of America, Washington, D.C., USA, pp. 463–483.

El Gh'Mari, A., 1995. Etude minéralogique, pétrophysique et géochimique de la dynamique d'altération d'un granite soumis aux dépôts atmosphériques acides (bassin versant du Strengbach, Vosges, France): mécanismes, bilans et modélisations, Université Louis Pasteur.

Eyring, H., 1935. The activated complex in chemical reactions. *J. Chem. Phys.* **3**, 107–115.

Fang, C., Moncrieff, J.B., 1999. A model for soil CO_2 production and transport 1: Model development. *Agri. For. Meteorol.* **95**, 225–236.

Fichter, J., 1997. Minéralogie quantitative et flux d'éléments minéraux libéré par altération des minéraux des sols dans deux écosystèmes sur granite (bassin versant du Strengbach, Vosges). Ph.D, Université Henri Poincaré, INRA.

Fichter, J., Dambrine, D., Turpault, M.-P., Ranger, J., 1998a. Base cation supply in spruce and beech ecosystems of the Strengbach catchment (Vosges mountains, N-E France). *Water Air Soil Poll.* **104**, 125–148.

Fichter, J., Turpault, M.-P., Dambrine, D., Ranger, J., 1998b. Localization of base cations in particle size fractions of acid forest soils (Vosges Mountains, N-E France). *Geoderma* **82**, 295–314.

Gautier, J.-H., Oelkers, E.H., Schott, J., 2001. Are quartz dissolution rates proportional to B.E.T. surface area? *Geochim. Cosmochim. Acta* **65**, 1059–1070.

Goddéris, Y., François, L.M., 1995. The Cenozoic evolution of the strontium and carbon cycles: relative importance of continental erosion and mantle exchanges. *Chem. Geol.* **126**, 169–190.

Goddéris, Y., Joachimski, M.M., 2004. Global change in the late Devonian: modelling the Frasnian-Famennian short-term carbon isotope excursions. *Palaeogeogr. Palaeoclimatol. Palaeoecol.* **202**, 309–329.

Golubev, S., Pokrovsky, O.S., Schott, J., 2005. Effect of dissolved CO_2 on the dissolution kinetics of basic silicates at 25 °C. *Chem. Geol.* **217**, 227–238.

Guidry, M.W., Mackenzie, F.T., 2003. Experimental study of igneous and sedimentary apatite dissolution: control of pH, distance from equilibrium, and temperature on dissolution rates. *Geochim. Cosmochim. Acta* **67**, 2949–2963.

Hodson, M.E., Langan, S.J., Meriau, S., 1998. Determination of mineral surface area in relation to the calculation of weathering rates. *Geoderma* **83**, 35–54.

Holmqvist, J., 2001. Modelling chemical weathering in different scales. Ph.D. thesis, Lund University, Lund.

Idir, S., Probst, A., Viville, D., Probst, J.L., 1999. Contribution des surfaces saturées et des versants aux flux d'eau et d'éléments exportés en période de crue: traçage à l'aide du carbone organique dissous et de la silice. Cas du petit bassin versant du Strengbach (Vosges, France). C.R. Acad. Sci. Paris 328, pp. 89–96.

Köhler, S.J., Dufaud, F., Oelkers, E.H., 2003. An experimental study of illite dissolution kinetics as a function of pH from 1.4 to 12.4 and temperature from 5 to 50 °C. *Geochim. Cosmochim. Acta* **67** (19), 3583–3594.

Kump, L.R., Arthur, M.A., 1997. Global chemical erosion during the Cenozoic: weatherability balances the budget. In: Ruddiman, W.F. (Ed.), *Tectonic and climate change*. Plenum Press, New York, pp. 399–426.

Kump, L.R., Brantley, S.L., Arthur, M.A., 2000. Chemical weathering, Atmospheric CO_2, and Climate. *Annu. Rev. Earth Planet. Sci.* **28**, 611–667.

Leuning, R., 1995. A critical appraisal of a combined stomatal-photosynthesis model for C3 plants. *Plant, Cell and Environment* **18**, 335–339.

Madé, B., Clément, A., Fritz, B., 1994. Modeling mineral/solution interactions: the thermodynamic and kinetic code KINDISP. *Computers and Geosciences* **20** (9), 1347–1363.

Mahfouf, J.F., Noilhan, J., 1991. Comparative study of various formulations of evaporation from bare soil using in situ data. *J. Appl. Meteorol.* **30**, 1354–1365.

Mast, M.A., Drever, J.I., Barron, J., 1990. Chemical weathering in the Loch Vale watershed, Rocky mountains National Park, Colorado. *Water Resour. Res.* **26**, 2971–2978.

Munhoven, G., 2002. Glacial-interglacial changes of continental weathering: estimates of the related CO_2 and HCO3 flux variations and their uncertainties. *Global Planet. Change* **33**, 155–176.

Nagy, K.L., 1995. Dissolution and precipitation kinetics of sheet silicates. In: White, A.F., Brantley, S.L. (Eds.), *Chemical Weathering Rates of Silicate Minerals, Reviews in Mineralogy*, Vol. 31. Mineralogical Society of America, Washington, D.C., USA, pp. 173–233.

Oelkers, E.H., Schott, J., Devidal, J.L., 1994. The effect of aluminum, pH and chemical affinity on the rates of aluminosilicate dissolution reactions. *Geochim. Cosmochim. Acta* **58**, 2011–2024.

Oliva, P., Dupré, B., Martin, F., Viers, J., 2004. The role of trace minerals in chemical weathering in a high-elevation granitic watershed (Estibère, France): chemical and mineralogical evidence. *Geochim. Cosmochim. Acta* **68** (10), 2223–2244.

Oliva, P., Viers, J., Dupré, B., 2003. Chemical weathering in granitic crystalline environments. *Chem. Geol.* **202**, 225–256.

Posch, M., Hettelingh, J.-P., Slootweg, J., 2003. Manual for dynamic modelling of soil response to atmospheric deposition, Rijksinstituut voor Volksgezondheid en Milieu, pp. 46–47.

Probst, A., Dambrine, D., Viville, D., Fritz, B., 1990. Influence of acid atmospheric inputs on surface water chemistry and mineral fluxes in a declining spruce stand within a small granitic catchment (Vosges massif, France). *J. Hydrol.* **116**, 101–124.

Probst, A., El Gh'Mari, A., Aubert, D., Fritz, B., McNutt, R., 2000. Strontium as a tracer of weathering processes in a silicate catchment polluted by acid atmospheric inputs, Strengbach, France. *Chem. Geol.* **170**, 203–219.

Probst, A., Fritz, B., Viville, D., 1995. Mid-term trends in acid precipitations, streamwater chemistry and element budgets in the Strengbach catchment (Vosges mountains, France). *Water Air Soil Poll.* **79**, 39–59.

Probst A., Viville D., 1997. Bilan hydrogéochimique du petit bassin versant forestier du Strengbach à Aubure (Haut Rhin). In *Rapport scientifique activités de recherche*, *5ème réunion du conseil de direction scientifique Ifare/DFIU, Conseil de l'Europe*, pp. 59–66.

Rasse, D.P., François, L.M., Aubinet, M., Kowalski, A.S., Vande Walle, I., Laitat, E., Gérard, J.C., 2001. Modelling short-term CO_2 fluxes and long-term tree growth in temperate forests with ASPECTS. *Ecol. Modell.* **141**, 35–52.

Rimstidt, J.D., 1997. Quartz solubility at low temperatures. *Geochim. Cosmochim. Acta* **61**, 2553–2558.

Schott, J., Oelkers, E.H., 1995. Experimental study of anorthite dissolution and the relative mechanism of feldspar hydrolysis. *Geochim. Cosmochim. Acta* **59**, 5039–5053.

Stefansson, A., Gislason, S.R., 2001. Chemical weathering of basalts, southwest Iceland: effect rock crystallinity and secondary minerals on chemical fluxes to the ocean. *Am. J. Sci.* **301**, 513–556.

Sverdrup, H., Hagen-Thorn, A., Holmqvist, J., Wallman, P., Warfinge, P., Walse, C., Alveteg, M., 2002. Biogeochemical processes and mechanisms. In: Sverdrup, H., Stjernquist, I. (Eds.), *Developing Principles and Models for Sustainable Forestry in Sweden*. Kluwer Academic Publishers, Dordrecht, pp. 91–196.

Sverdrup, H., Warfinge, P., 1995. Estimating field weathering rates using laboratory kinetics. *Rev. Mineral.* **31**, 485–541.

Tagirov, B., Schott, J., 2001. Aluminum speciation in crustal fluids revisited. *Geochim. Cosmochim. Acta* **65**, 3965–3992.

Tardy, Y., Garrels, R.M., 1974. A method of estimating the Gibbs energies of formation of layer silicates. *Geochim. Cosmochim. Acta* **38**, 1101–1116.

Vieillard, P., 2000. A new method for the prediction of Gibbs free energies of formation of hydrated clay minerals based on the electronegativity scale. *Clays Clay Miner.* **48**, 459–473.

Viterbo, P., Beljaars, C.M., 1995. An improved land surface parametrization scheme in the ECHWF model and its validation. *J. Clim.* **8**, 2716–2748.

Walker, J.C.G., Hays, P.B., Kasting, J.F., 1981. A negative feedback mechanism for the long-term stabilization of Earth's surface temperature. *J. Geophys. Res.* **86**, 9776–9782.

Wallman, P., Svensson, M.G.E., Sverdrup, H., Belyazid, S., 2005. ForSAFE-an integrated process-oriented forest model for long term sustainability assessments. *Forest Ecol. Manag.* **207**, 19–36.

Wallman, P., Sverdrup, H., Svensson, M.G.E., Alveteg, M., 2002. Integrated modelling. In: Sverdrup, H., Stjernquist, I. (Eds.), *Developing Principles and Models for Sustainable Forestry in Sweden*. Kluwer Academic Publisher, Dordrecht, pp. 57–83.

Walther, J.V., Hegelson, H.C., 1977. Calculation of the thermodynamic properties of aqueous silica and the solubility of quartz and its polymorphs at high pressures and temperatures. *Am. J. Sci.* **277**, 1315–1351.

Warfinge, P., Sverdrup, H., 1998. Soil liming as a measure to mitigate acid runoff. *Water Resour. Res.* **24**, 701–712.

Wesolowski, D.J., Palmer, D.A., 1994. Aluminium speciation and equilibria in aqueous solution: V. Gibbsite solubility at 50 °C and pH 3–9 in 0.1 molal NaCl solutions. *Geochim. Cosmochim. Acta* **58**, 2947–2970.

White, A.F., Blum, A.E., 1995. Effects of climate on chemical weathering in watersheds. *Geochim. Cosmochim. Acta* **59**, 1729–1747.

White, A.F., Bullen, T.D., Davison, V.V., Schulz, M.S., Clow, D.W., 1999. The role of disseminated calcite in the chemical weathering of granitoid rocks. *Geochim. Cosmochim. Acta* **63**, 1939–1953.

White, A.F., Schulz, M.S., Lowenstern, J.B., Vivit, D.V., Bullen, T.D., 2005a. The ubiquitous nature of accessory calcite in granitoid rocks: implications for weathering, solute evolution, and petrogenesis. *Geochim. Cosmochim. Acta* **69** (6), 1455–1471.

White, A.F., Schulz, M.S., Vivit, D.V., Blum, A.E., Stonestrom, D.A., Harden, J.F., 2005b. Chemical weathering rates of a soil chronosequence on granitic alluvium: III. Hydrochemical evolution and contemporary solute fluxes and rates. *Geochim. Cosmochim. Acta* **69**, 1975–1996.